Phase microstructure and morphology evolution of MgO-PSZ ceramics during the microwave sintering process

Qiannan Li [a], Yeqing Ling [a], Hewen Zheng [a], Guo Chen [a, **], Jin Chen [a], Sivasankar Koppala [b], Qi Jiang [a], Kangqiang Li [a], Mamdouh Omran [c], Lei Gao [a, *]

[a] *Kunming Key Laboratory of Energy Materials Chemistry, Key Laboratory of Green-Chemistry Materials in University of Yunnan Province, Yunnan Minzu University, Kunming 650500, P.R. China.*

[b] *Panjin Institute of Industrial Technology, Dalian University of Technology, Panjin 124221, Liaoning, P.R. China.*

[c] *Process Metallurgy Research Group, Faculty of Technology, University of Oulu, Finland.*

[*] Corresponding author: glkust2013@hotmail.com

[**] Co-corresponding author: guochen@kust.edu.cn

Abstract:

In the present study, controllable microwave sintering was applied to prepare partially stabilised zirconia ceramics with enhanced phase composition and a more uniform structure. To reveal the phase interface properties and structural changes of PSZ ceramics during the microwave sintering process, XRD, FT-IR, Raman, and SEM characterisations were utilised. XRD analysis and Raman analysis demonstrated that the increase of sintering temperature promoted the martensite conversion. However, prolonging duration time was unconducive to the retention of the stable phase. Additionally, the FT-IR characteristic peak movement caused by the reversible phase martensite transformation was observed. Furthermore, SEM analysis found that microwave treatment improved the grain size and structure distribution of the as-received MgO-PSZ sample. This work constructed a controllable technical prototype of preparing PSZ ceramics via microwave sintering, which can provide a theoretical basis and experimental basis for further industrial production.

Keywords: MgO-PSZ ceramics; microwave sintering; phase microstructure; surface morphology

1 Introduction

Zirconia (ZrO_2) has widely been applied as ceramic coatings, high-temperature parts, and structural ceramic materials, etc., which is attributed to its distinct physical-chemical performances including low thermal conductivity, high hardness, high thermal stability, and high melting point [1-4]. During the phase change process of ZrO_2 where the lattice of ZrO_2 material is modified without the composition variation, the conversion between monoclinic

phase (m-ZrO_2) and tetragonal phase (t-ZrO_2) is reversible. Therefore, the phase change of ZrO_2 is considered as martensite transformation [5-8]. However, pure ZrO_2 material presents a volume change effect in the reversible martensite transformation process between the monoclinic phase and tetragonal crystals [9-11]. The volume change effect is mainly manifested by the 5% volume expansion in the cooling process and the 3.25% volume shrinkage in the heating process, resulting in the accumulation of tensile stress inside pure ZrO_2 material and further cause the cracking of its products, which seriously limits the application of pure ZrO_2 materials [12-13]. Therefore, pure ZrO_2 needs to be stabilised to achieve a toughening effect.

Currently, the toughening effect of ZrO_2 materials is mainly achieved through doping stabilisers [14-15]. By adding the appropriate stabiliser, the phase transition temperatures of the monoclinic crystal (m) into tetragonal crystal (t) and tetragonal crystal (t) into cubic crystal (c) can be reduced. Meanwhile, cubic and tetragonal crystals that exist stably under high temperature can also be stable or meta-stable at room temperature. The crystalline stability of the ZrO_2 materials doped with stabiliser produces the phase change of tetragonal into the monoclinic crystal, induced by stress when bearing [16]. Attributed to the volume effect produced by the phase transition of t-ZrO_2→m-ZrO_2, a lot of fracture energy is absorbed. The material exhibits abnormally high fracture toughness, rendering the doped ZrO_2 materials toughen with high toughness and high wear resistance characteristics [17]. Commonly, the doped stabilisers are mainly alkaline-earth and rare earth oxides. Meanwhile, the difference in radius between the oxides' ionic and Zr^{4+} should be less than 40% [18]. Notably, MgO [19], CaO [20], Y_2O_3 [21] and CeO_2 [22] are more commonly used. The

stability mechanism is generally explained as: the cations of stabilisers such as Mg^{2+}, Ca^{2+}, Ce^{4+}, and Y^{3+} have certain solubility in ZrO_2 material. Therefore, those cations can replace Zr^{4+} and form a solid replacement solution, which hinders the transition of tetragonal crystal to monoclinic crystal, reducing the transition temperature of tetragonal crystal into the monoclinic crystal and making tetragonal crystal metastable to room temperature [23-24]. Through controlling the type, amount or grain size of the doped stabiliser, ZrO_2 material with different forms of stable state can be obtained, and it is generally divided into three kinds: tetragonal zirconia polycrystalline (TZP), full stabilised zirconia (FSZ), and partially stabilised zirconia (PSZ) [25-26]. PSZ materials contain a phase-changeable tetragonal phase, which is commonly used as phase change toughening ceramic materials. At present, the preparation of PSZ ceramics mainly adopts the electric heating method. However, due to the problems of high temperature (above 1450 °C), long operation time, and serious heat loss during the heating process, the sintering performance of PSZ ceramics prepared is unstable, limiting the development and application of PSZ ceramics materials [16]. Therefore, new methods for preparing PSZ ceramics are urgently needed to be explored, expecting to realise the control of the performance of PSZ ceramics.

Microwave heating technology has become a burgeoning technical means for quickly preparing high-performance new materials and modifying conventional materials, based on the special energy transfer and conversion mechanism, as well as rapid heating and selective heating characteristics [27-30]. Guo et al. [31] explored the microwave heating characteristics of fused ZrO_2. They reported that fused ZrO_2 was heated to 1475 °C within 4 min. The finding denotes the feasibility of applying microwave heating means on ZrO_2 ceramics

preparation. Nightingale et al. [32] investigated the microstructure change of Y_2O_3-doped ZrO_2 ceramics. They highlighted that the microwave sintered sample had more dense microstructures compared to conventionally heated samples. Benavente et al. [33] utilised microwave sintering means to synthesise Al_2O_3-ZrO_2 nanocomposites. The study results indicated that in comparison to conventional heating, higher Young′s modulus, density, and hardness, homogeneous microstructure, and excellent fracture toughness properties were obtained. Microwave heating is different from the heat conduction process of conventional heating, with high heating efficiency; therefore, applying microwave heating as an alternative means of conventional heating has significant advantages in energy saving and emission reduction for the transformation of high energy-consuming industries [34-36]. Meanwhile, microwave heating can improve the uniformity and yield of products and optimise the microstructure and performance of the processed materials [37-39].

In this work, focusing on the key issues in the efficient utilisation and quality improvement of ZrO_2 material, the special energy transfer and energy conversion method of microwave sintering means were fully used to prepare PSZ ceramics, using fused ZrO_2 as the research object and magnesium oxide (MgO) as the stabiliser, aiming to solve the technical problems of low product quality controllability, high process temperature and long operation time during the conventional preparation process of PSZ ceramics. Meanwhile, the transformation and evolution of the components of the multi-phase complex system in fused ZrO_2 under microwave action were studied. The influences of sintering temperature and duration time on the phase interface properties and structural changes of MgO-doped PSZ ceramics were discussed.

2 Materials and methods

2.1 Materials

The ZrO_2 raw material was sourced from a factory in Zhengzhou City, Henan Province, China. The chemical component analysis of the fused ZrO_2 sample was detailed as follows (%/(w/w): ZrO_2, 92.4; MgO, 4.0; SiO_2, 2.3; Al_2O_3, 1.0; TiO_2, 0.2; Fe_2O_3, 0.1, respectively. It was extracted that the main components of the fused ZrO_2 sample were ZrO_2 and MgO phases, wherein the MgO phase was the doped stabiliser. Additionally, Fig. 1 illustrated the Raman spectra and XRD pattern of the fused ZrO_2 sample. As presented in Fig. 1(a), it was determined that in the fused ZrO_2 sample, cubic crystal (JCPDS: 49-1642) and monoclinic crystal (JCPDS: 37-1484) undoubtedly existed, but there was an absence of the diffraction peak of MgO phase detected, signifying that the stable replacement solid solution structure was formed, with MgO stabiliser entering the lattice node of ZrO_2. Moreover, tetragonal crystal (JCPDS: 42-1164) and cubic crystal overlapped at the diffraction peaks of 2θ=30.18 °and 2θ=35.15 °. Therefore, it can be confirmed that in the MgO-doped ZrO_2 sample, there contained a cubic phase and a monoclinic phase of ZrO_2. However, the tetragonal phase of ZrO_2 cannot be determined, which needed another analysis method like Raman characterisation to test. Besides, from the Raman spectra of the fused ZrO_2 sample (Fig. 1(b)), three characteristic peaks caused by the Raman vibration arose at 285.2 cm^{-1}, 374.8 cm^{-1}, and 403.5 cm^{-1}, respectively. Among the three characteristic peaks, the peaks at 374.8 cm^{-1} and 403.5 cm^{-1} were due to m-ZrO_2 phases' B_g vibration, the peak at 285.2 cm^{-1} was caused by tetragonal crystals' E_g vibration, denoting that minority tetragonal crystal

existed in the raw material. In summary, the fused ZrO_2 sample can be classified as Partially Stabilised Zirconia (PSZ), with MgO doped as the stabiliser, which is also named magnesium oxide-doped partially stabilised zirconia (MgO-PSZ) ceramics material.

2.2 Instrumentation

The sintering experiments for the fused ZrO_2 materials were furnished in the high-temperature microwave box reactor (RWS-6, Hunan Thersun Thermal Energy Technology Co., Ltd.). The microwave reactor mainly included a microwave oven cavity, microwave energy feeding system, cooling water machine, thermal insulation system, air extraction system, intelligent control system, infrared thermometer, and other auxiliary equipment.

2.3 Characterisation

The change in phase, surface morphology, and microstructure of magnesia-doped PSZ ceramics during the microwave sintering process were explored through the comparison between the raw ZrO_2 samples with and without sintering treatment by microwaves, using XRD, Raman, FT-IR, and SEM characterisations. Wherein the X-ray diffractometer (D8 ADVANCE A25×, Bruker, Germany) was utilised to characterise the phase evolution of MgO-PSZ samples, with Cu target Ka-ray (λ=1.54056 Å) as the target source; the Confocal Raman spectrometer (InVia, Renishaw, UK) was used to perform the chemical structures of MgO-PSZ samples, scattering between the spectral detection area of 100 cm^{-1}-800 cm^{-1}; the Fourier infrared spectrometer (NICOLET-IS10, American) was responsible for determining the surface functional groups of MgO-PSZ samples, attaching the scanning spectral regime of 4000 cm^{-1}-500 cm^{-1}; also, the scanning electron microscope (XL30ESEM-TM, Philips, Netherlands) was utilised to observe the microstructures of MgO-PSZ samples.

2.4 Procedure

The raw MgO-PSZ material was firstly dried under 105 °C by a drying oven (FX101-1) lasting for 12 h. Then, the dried raw material was sampled using an electronic balance (AL-104) with a mass of 50.0 g, followed by the weighted sample was transformed into the high-temperature microwave box reactor. The sintering experimental parameters were detailed as follows: sintering temperature was adjustable among 900 °C, 1000 °C, 1100 °C, and 1200 °C, duration time was adjustable among 1 h, 2 h, 3 h, and 4 h, and microwave heating power was maintained at 3 kW. Once the sintering experimental parameters reached the set values, the high-temperature microwave box reactor stopped working. The sintered samples were naturally cooled in the microwave reactor and collected for characterisation analysis.

3 Results and discussion

Sintering temperature and duration time present great influences on the performance and microstructure of MgO-doped PSZ ceramics samples. Through adjusting sintering temperature and duration time, the phase microstructure and morphology evolution of MgO-doped PSZ ceramics during the microwave sintering process were unveiled using XRD, Raman, FT-IR, and SEM characterisations, further contribute to determining the technological conditions of the microwave sintering approach.

3.1 XRD characterisation

3.1.1 Influence of sintering temperature

The XRD patterns of the synthesised MgO-PSZ samples under various microwave sintering temperatures were depicted in Fig. 2, wherein the duration time was constant at 1 h.

As illustrated in Fig. 2, under microwave processing at 900 °C for 1 h, the main phases in the sintered sample were strong monoclinic and cubic crystals. The diffraction peaks at 2θ=30.12°, 2θ=50.22°, and 2θ=34.96° belonged to cubic crystal. The diffraction peaks exactly corresponded to the (111), (200) and (220) three strong crystal planes of c-ZrO_2 phase; and m-ZrO_2 phases' diffraction peaks emerged at 2θ=28.06° and 2θ=31.24°. In contrast to the raw material, the diffraction peaks of the MgO-PSZ sample sintered at 900 °C were absent of obvious refinement, with small miscellaneous peaks. This finding manifested that under this experimental condition (at 900 °C for 1 h), the sample crystal structure was defective. The crystal structure of some samples was still in the amorphous phase, accompanied by the phase change reaction had not started in the sample. As temperature lifted to 1000 °C, the peak intensity at 2θ=30.12° belonging to cubic crystal was significantly enhanced. Meanwhile, m-ZrO_2 phase diffraction peaks' intensities at 2θ=28.06° and 2θ=31.24° were also enhanced. The two diffraction peaks exactly corresponded to the (111) crystal plane of the c-ZrO_2 phase. Compared to the MgO-PSZ sample sintered at 900 °C, the intensities of each characteristic peak became larger. The peak shape was refined, indicating that the grains had better development under 1000 °C.

With the temperature rising to 1100 °C, c-ZrO_2 phases' peak intensities continued to increase, and m-ZrO_2 phases' peak intensities gradually decreased, as presented in Fig. 2. The diffraction peaks of the stable phase gradually refined with temperature improving, indicating that the transformation of m-ZrO_2 into t-ZrO_2 began. As temperature improved to 1200 °C, the m-ZrO_2 phase disappeared, indicating that increasing sintering temperature promoted the added magnesium ions gradually entered the ZrO_2 lattice and acted on the magnesium ions

(Mg^{2+}) [14, 18]. Meanwhile m-ZrO_2 phase was transformed into the t-ZrO_2 phase and kept it to room temperature, further to render the gradual decrease of the content of m-ZrO_2 phase. Also, the m-ZrO_2 phases' diffraction peak disappeared at 1200 °C, as shown in Fig. 2. According to the calculation formula of the stability rate of ZrO_2 ceramics material [40], the stability rate obtained under a temperature of 1200 °C was highest among those sintering temperatures. Hence, the favourable sintering temperature could be considered at 1200 °C.

3.1.2 Influence of duration time

Maintaining the sintering temperature constant at 1200 °C and controlling duration time among the regime of 1 h~4 h, influences of duration time on the phase change were explored, and the results were depicted in Fig. 3. As shown in Fig. 3, after sintering treatment at 1200 °C for 1 h, the diffraction peaks of the three strong (111), (200) and (220) crystal planes of c-ZrO_2 phase arose at 2θ=30.12°, 2θ=50.220° and 2θ=34.960°, meanwhile the intensities of the diffraction peaks were very high. In contrast to the raw ZrO_2 sample, monoclinic crystal vanished, denoting that the phase conversion of the ZrO_2 sample was complete under those conditions, with a large amount of monoclinic crystal converted to tetragonal crystal, and the grains of the c-ZrO_2 phase gradually grew. As duration time prolonged to 2 h, c-ZrO_2 phases' diffraction peak intensity in the sample significantly enhanced. However, the m-ZrO_2 phase diffraction peaks appeared at 2θ=28.06° and 2θ=31.24°. The experimental phenomenon indicated that prolonging duration time promoted the growth of the grains of the c-ZrO_2 phase and the reversible transformation between t-ZrO_2 and m-ZrO_2 phases.

As duration time prolonged to 3 h, the peak intensity belonging to the (111) crystal plane of c-ZrO_2 phase significantly increased; in contrast, m-ZrO_2 phases' peak intensities at

2θ=28.06° and 2θ=31.24° did not change much, indicating that c-ZrO_2 phase grains grew well with the extension of duration time. With duration time continually improving to 4 h, c-ZrO_2 phases' peak intensities had weakened, especially the XRD diffraction peaks located at 2θ=30.12°, 2θ=50.22°, and 2θ=34.96°. Furthermore, the intensity of the m-ZrO_2 phase diffraction peak became enhanced, compared to the MgO-doped PSZ sample synthesised under a duration time of 3 h. Therefore, it can be summed that the extension of duration time was unconducive to the retention of the stable phase, and the favourable duration time could be considered at 1 h.

3.2 Raman characterisation

3.2.1 Influence of sintering temperature

Controlling the duration time constant at 1 h and varying sintering temperature among 900 °C to 1200 °C, influences of sintering temperature on the chemical structure were explored, and the obtained Raman spectra were plotted in Fig. 4. As illustrated in Fig. 4(a), the Raman spectra of the sample were synthesised at 900 °C and the Raman spectra of the sample showed the strongest peak at 403.5 cm^{-1}, the second strongest peaks appeared at 285.8 cm^{-1} and 374.8 cm^{-1}, and a medium intensity peak at 317.6 cm^{-1}. The Raman vibration characteristic peaks at 285.8 cm^{-1} and 317.6 cm^{-1} belonged to the t-ZrO_2 phase. The Raman peaks located at 374.8 cm^{-1} and 403.5 cm^{-1} belonged to the m-ZrO_2 phase. Besides, as presented in Fig. 4(a), the Raman activity of monoclinic crystal and tetragonal crystal appeared. Meanwhile, the corresponding XRD pattern (Fig. 2) denoted that there was an amorphous phase at this temperature (900 °C), indicating that there was relatively minority tetragonal crystal. Moreover, in contrast to the raw ZrO_2 sample, the peak intensities of the

two phases were not very high, indicating that the transformation of monoclinic crystal into tetragonal crystal was not intense under the temperature of 900 °C. With the temperature increasing to 1000 °C, six Raman vibration characteristic peaks appeared in the Raman spectrum of the MgO-PSZ sample, located at 648.8 cm^{-1}, 403.5 cm^{-1}, 374.8 cm^{-1}, 317.6 cm^{-1}, 285.8 cm^{-1}, and 147.4 cm^{-1}, respectively, as depicted in Fig. 4(b). Wherein the Raman peaks caused by the B_g and E_g Raman vibrations of tetragonal crystal located at 317.6 cm^{-1}, 147.4 cm^{-1}, 285.8 cm^{-1}, and 646.8 cm^{-1}; and the Raman peak at 403.5 cm^{-1} resulted in the B_g Raman vibration of the monoclinic crystal. Compared with the MgO-doped PSZ sample synthesised at 900 °C, the relative intensities of the Raman vibration characteristic peak in the MgO-PSZ sample sintered at 1000 °C significantly enhanced and became sharp, indicating that the conversion of monoclinic crystal into tetragonal crystal started, further to cause the content of tetragonal crystal increased.

As the temperature rose to 1100 °C, eight Raman vibration characteristic peaks appeared, as presented in Fig. 4(c). The four peaks at 317.6 cm^{-1}, 147.4 cm^{-1}, 285.8 cm^{-1}, and 646.8 cm^{-1} were assigned to tetragonal crystals' B_g and E_g Raman vibrations. The Raman peak at 403.5 cm^{-1} resulted in the B_g Raman vibration of the monoclinic crystal. At this temperature, the Raman vibration modes of the t-ZrO_2 phase were more obvious, but the m-ZrO_2 phase' peak intensity was weakened at 403.5 cm^{-1}, indicating that the content of the m-ZrO_2 phase had decreased. The phenomenon denoted that a certain amount of the stable phase in the sample was stored till room temperature, and it did not transform into the m-ZrO_2 phase. With temperature continually lifting to 1200 °C, the strongest peak arose at 403.7 cm^{-1}, the secondary strongest peaks appeared at 286.0 cm^{-1} and 376.9 cm^{-1}, and the moderate-intensity

peaks arose at 147.6 cm^{-1}, 321.0 cm^{-1}, and 645.4 cm^{-1}, as illustrated in Fig. 4(d). In contrast to the MgO-doped PSZ sample synthesised at 1100 °C (Fig. 4(c)), the intensities of the Raman peaks at 286.0 cm^{-1} and 321.0 cm^{-1} belonging to tetragonal crystal enhanced with the temperature rising. Meanwhile, some characteristic peaks disappeared, signifying that the increase in temperature contributed to the phase transition of monoclinic crystal into the tetragonal crystal, further reducing the monoclinic crystal phase. The conclusions concluded from the Raman spectra analysis corresponded to the XRD pattern (Fig. 2).

3.2.2 Influence of duration time

Maintaining temperature constant at 1200 °C and varying duration time from 1 h to 4 h, influences of duration time on the chemical structure were probed, and the Raman spectra were depicted in Fig. 5. After sintering at 1200 °C lasting for 1 h, six Raman activities were detected in the Raman spectrum of the sample, located at 403.7 cm^{-1}, 286.0 cm^{-1}, 376.9 cm^{-1}, 147.6 cm^{-1}, 321.0 cm^{-1}, and 645.4 cm^{-1}, as presented in Fig. 5(a). The characteristic peaks caused by the B_g and E_g Raman vibrations of the t-ZrO_2 phase are 147.6 cm^{-1}, 286.0 cm^{-1}, 321.0 cm^{-1}, and 645.4 cm^{-1}, the characteristic peaks assigned to the B_g Raman vibration of m-ZrO_2 phase are 376.9 cm^{-1} and 403.7 cm^{-1}. Referring to the raw ZrO_2 material, the m-ZrO_2 phase's content in the MgO-PSZ sample under 1200 °C decreased, which was attributed to the convection of a large amount of m-ZrO_2 phase into the t-ZrO_2 phase. With duration time prolonging to 2 h, the strongest peak arose at 403.7 cm^{-1}, and other strong peaks arose at 286.0 cm^{-1}, 375.1 cm^{-1}, 147.6 cm^{-1}, and 645.4 cm^{-1}, as displayed in Fig. 5(b). By comparison with Fig. 5(a), it was observed that with the extension of a duration time, the relative

intensities of the peaks including 147.6 cm^{-1}, 286.0 cm^{-1}, and 645.4 cm^{-1} decreased, indicating the content of the t-ZrO_2 phase decreased.

As duration time extended to 3 h, the Raman peaks including 149.0 cm^{-1}, 287.3 cm^{-1}, and 643.6 cm^{-1} were attributed to t-ZrO_2 phases' Raman vibration, and the Raman peaks at 376.4 cm^{-1} and 401.8 cm^{-1} were caused by m-ZrO_2 phases' Raman vibration. Under the conditions of the holding time of 3 h, t-ZrO_2 phases' characteristic peaks intensities were significantly weakened compared with Fig. 5(b), denoting t-ZrO_2 phase content decreased with the extension of duration time. Meanwhile, the peak frequencies of the Raman vibration peaks at 149.0 cm^{-1}, and 287.3 cm^{-1} shifted to a high wave number, resulting in a blue shift. As duration time prolonged to 4 h, the Raman spectrum of the sintered MgO-PSZ sample showed five Raman active vibrations, as presented in Fig. 5(d). Referring to Fig. 5(c), the Raman activities in the sample were the same, only the position of the Raman peaks had changed slightly. The Raman vibration characteristic peaks of the t-ZrO_2 phase continued to weaken, only reaching about 4500 (a.u.). The Raman spectra analysis indicated that extending duration time was conductive to the phase transition of monoclinic crystal into the tetragonal crystal, further to render tetragonal crystal decreased. The findings obtained from Raman spectra also matched the XRD pattern (Fig. 3).

3.3 FT-IR characterisation

3.3.1 Influence of sintering temperature

Maintaining duration time constant at 1 h and controlling sintering temperature regime of 900 °C~1200 °C, effects of sintering temperature on the microscopic surface functional groups of the magnesia-doped PSZ samples were investigated, and the FT-IR spectra were

plotted in Fig. 6. As displayed in Fig. 6, five FT-IR characteristic peaks were detected in the raw fused ZrO_2 sample, including 3447.56 cm^{-1}, 1643.53 cm^{-1}, 1416.46 cm^{-1}, 1013.39 cm^{-1} and 545.50 cm^{-1}. Specifically, the FT-IR peak at 545.50 cm^{-1} resulted in the Zr-O bonds' contraction vibration; the characteristic peak at 1013.39 cm^{-1} was due to the O-H bonds' bending vibration; the FT-IR peak at 1416.46 cm^{-1} was assigned to the sample adsorbs carbon dioxide (CO_2) in the air; the characteristic peaks at 1643.53 cm^{-1} were attributed to H-O-H bonds' bending vibration. The H-O-H bonds were generated by the sample absorbs water molecules in the air; and the FT-IR peak at 3447.56 cm^{-1} resulted in the O-H bonds' contraction vibration.

After sintering at 900 °C for 1h, the infrared spectroscopy peaks at 546.14 cm^{-1}, 1011.31 cm^{-1}, 1416.97 cm^{-1}, 1641.25 cm^{-1}, and 3448.15 cm^{-1} appeared in the sintered MgO-PSZ sample. Compared with the raw ZrO_2 sample, the wavenumbers of the five FT-IR peaks hardly changed. With temperature rising to 1000 °C, the five FT-IR peaks arose, including 3448.67 cm^{-1}, 1617.52 cm^{-1}, 1400.66 cm^{-1}, 1068.09 cm^{-1}, and 477.95 cm^{-1}, respectively. Besides, the FT-IR peak at 477.95 cm^{-1} was assigned to the stretching vibration of the Zr-O bonds, which is the FT-IR peak of the t-ZrO_2 phase; meanwhile, by the comparison between the raw material and the MgO-PSZ sample sintered at 900 °C, it can be concluded that the characteristic peak frequency shifted to a low wavenumber, resulting in a red shift. Notably, the red shift was induced by that monoclinic phase that started to convert into a tetragonal phase with a temperature rising. As temperature improved to 1100 °C, the five FT-IR peaks arose at 3448.83 cm^{-1}, 1617.32 cm^{-1}, 1416.27 cm^{-1}, 1067.04 cm^{-1}, and 514.36 cm^{-1}, respectively. Referring to the MgO-PSZ sample sintered at 1000 °C, the first infrared peak

moved from 477.95 cm^{-1} to 514.36 cm^{-1}, toward a high wavenumber, resulting in a blue shift. The blue shift of the FT-IR peak was ascribed to the continuous conversion process of monoclinic crystal into tetragonal crystal rendered tetragonal crystal increased in the sintered MgO-PSZ sample. With temperature improving to 1200 °C, the five FT-IR peaks moved to 3447.66 cm^{-1}, 1617.55 cm^{-1}, 1400.37 cm^{-1}, 1066.77 cm^{-1}, and 513.11 cm^{-1}, respectively. Meanwhile, the wavenumbers of the five peaks had not changed much with the comparison to the MgO-PSZ sample sintered at 1100 °C, denoting that the conversion process of m-ZrO_2 into t-ZrO_2 gradually tended to be gentle.

3.3.2 Influence of duration time

Controlling the sintering temperature at 1200 °C and varying holding time among 1 h to 4 h, effects of duration time on the microscopic surface functional groups of the MgO-PSZ samples were presented in Fig. 7. As displayed in Fig. 7, in the magnesia-doped PSZ sample synthesised at 1200 °C, five FT-IR peaks were detected at 3447.66 cm^{-1}, 1617.55 cm^{-1}, 1400.37 cm^{-1}, 1066.77 cm^{-1}, and 513.11 cm^{-1}, respectively. As duration time prolonged to 2 h, the five FT-IR peaks moved to 3447.05 cm^{-1}, 1617.26 cm^{-1}, 1400.37 cm^{-1}, 1066.08 cm^{-1}, and 513.43 cm^{-1}, respectively, with little change; in addition, under the duration time of 3 h, the five peaks correspondingly changed to 3447.28 cm^{-1}, 1617.07 cm^{-1}, 1400.06 cm^{-1}, 1067.88 cm^{-1}, and 513.16 cm^{-1}, without significant change. Similarly, with the duration time prolonging to 4 h, the characteristic peak caused by the Zr-O bonds' stretching vibration moved from 513.16 cm^{-1} to 516.08 cm^{-1}, towards a high wavenumber, resulting in a blue shift. The blue shift indicated that the continuous process of the phase conversion of monoclinic

crystal into tetragonal crystal rendered the increase of the content of tetragonal crystal in the sintered magnesia-doped PSZ sample.

3.4 SEM characterisation

3.4.1 Influence of sintering temperature

SEM images of the synthesised magnesia-doped PSZ samples under various sintering temperatures for 1 h were displayed in Fig. 8, determined using the same magnification of 5000 x. As illustrated in Figs. 8(a) and (b), the surface of the raw fused ZrO_2 sample was smooth, and the particle shape was irregular. After microwave sintering at 900 °C, the sample size became larger and a small number of grains accumulated on the surface (Fig. 8(c)); meanwhile, the particle clumping phenomenon appeared with a temperature rising to 1000 °C, a large number of grains accumulated and the sample began to crystallise (Fig. 8(d)), denoting the phase transition of monoclinic crystal into tetragonal crystal accompanied with the increase of sintering temperature. Additionally, as sintering temperature continually improved to 1100 °C, the edges of the particles began to become smooth, the particles aggregated with each other, and some particles grew abnormally (Fig. 8(e)); furthermore, with temperature reached 1200 °C, the sample surface became smoother, fine grains and no pores arose, and the grain size became more uniform (Fig. 8(f)). The uniform structure of the synthesised magnesia-doped PSZ sample by microwave sintering indicated that the added MgO stabiliser promoted the fusion of crystal grains in ZrO_2 ceramics material, further highlighting that microwave sintering is an effective approach to prepare PSZ ceramics material.

3.4.2 Influence of duration time

SEM images of the synthesised magnesia-doped PSZ samples under microwave radiation at 1200 °C with different durations were presented in Fig. 9, characterised using the same magnification of 5000 x. Under microwave sintering with the duration time of 1 h, a large number of grains were accumulated in the sample, and no pores were generated, as illustrated in Fig. 9(a). Under the duration time of 2 h, there was a partial agglomeration between the grains, and the grain surface became smooth, as illustrated in Fig. 9(b). Besides, as displayed in Fig. 9(c), individual grains in the sample presented prominent growth phenomena with duration time increasing to 3 h. The prominent growth phenomena promoted the grain size to become non-uniform. With duration time continually increasing to 4 h, the grain surface of the synthesised magnesia-doped PSZ sample became smoother, the densification was better, and no pores were generated, as presented in Fig. 9(d). The sintered MgO-PSZ ceramic material with the smoother and denser microstructure indicated microwave sintering approach presented the prominent sintering effect on the fused ZrO_2 material. The approach can be extended to the sintering preparation of other ceramic materials.

4 Conclusions

In the present work, the change in phase, surface morphology, and microstructure of magnesia-doped PSZ ceramics during the microwave sintering process were systematically explored. XRD analysis results denoted that the c-ZrO_2 phase enhanced and the m-ZrO_2 phase gradually weakened until disappeared with the increase of sintering temperature from 900 °C to 1200 °C; however, the m-ZrO_2 phase reappeared with duration time extending, which was

caused by ZrO_2 materials' unique martensitic transformation. Moreover, the conclusions concluded from Raman analysis corresponded to XRD analysis results. Additionally, the reversible martensitic transformation induced a red shift at 1000 ℃ and a blue shift at 1100 ℃ about the FT-IR characteristic peak caused by the Zr-O bonds' contraction vibration. Furthermore, after the raw fused ZrO_2 sample through microwave sintering, the sample surface became smoother surface and the microstructure was more uniformly distributed. This study highlights that microwave sintering means is remarkably effective on the transformation toughening of fused ZrO_2 and the controllable production of high-performance PSZ ceramics.

Acknowledgements

Financial support from National Natural Science Foundation of China (Grant No. 51764052), and Innovative Research Team (in Science and Technology) in the University of Yunnan province.

References

1. C. Patapy, F. Gouraud, M. Huger, R. Guinebretière, B. Ouladiaff, D. Chateigner, T. Chotard, Investigation by neutron diffraction of texture induced by the cooling process of zirconia refractories, J. Eur. Ceram. Soc. 34(15) (2014) 4043-4052. https://doi.org/10.1016/j.jeurceramsoc.2014.05.027.
2. K.Q. Li, Q. Jiang, J. Chen, J.H. Peng, X.P. Li, S. Koppala, M. Omran, G. Chen, The controlled preparation and stability mechanism of partially stabilised zirconia by microwave intensification, Ceram. Int. 46(6) (2020) 7523-7530. https://doi.org/10.1016/j.ceramint.2019.11.251.

3. F. A. Kroger, Electronic conductivity of calcia-stabilised zirconia, J. Am. Ceram. Soc. 49(4) (2010) 215-218. https://doi.org/10.1111/j.1151-2916.1966.tb13237.x.

4. G. Chen, Y.Q. Ling, Q.N. Li, H.W. Zheng, K.Q. Li, Q. Jiang, J. Chen, M. Orman, L. Gao, Crystal structure and thermomechanical properties of CaO-PSZ ceramics synthesised from fused ZrO_2, Ceram. Int. 46(10) (2020) 15357-15363. https://doi.org/10.1016/j.ceramint.2020.03.079.

5. M. Mamivand, M.A. Zaeem, H.E. Kadiri, Effect of variant strain accommodation on the three-dimensional microstructure formation during martensitic transformation: Application to zirconia, Acta. Mater. 87 (2015) 45-55. https://doi.org/10.1016/j.actamat.2014.12.036.

6. X.M. Zeng, A. Lai, C.L. Gan, C.A. Schuh, Crystal orientation dependence of the stress-induced martensitic transformation in zirconia-based shape memory ceramics, Acta. Mater. 116 (2016) 124-135. https://doi.org/10.1016/j.actamat.2016.06.030.

7. Y. Q. Ling, Q. N. Li, H. W. Zheng, M. Omran, L. Gao, J. Chen, G. Chen, Optimisation on the stability of CaO-doped partially stabilised zirconia by microwave heating, Ceram. Int. (2020). https://doi.org/10.1016/ j.ceramint.2020.11.161.

8. K. Q. Li, Q. Jiang, G. Chen, L. Gao, J. H. Peng, Q. Chen, S. Koppala, M. Omran, J. Chen, Kinetics characteristics and microwave reduction behaviour of walnut shell-pyrolusite blends, Bioresour. Technol. 319 (2021) 124172. https://doi.org/10.1016/j.biortech.2020.124172.

9. P.E. Reyes-Morel, I.W. Chen, Transformation plasticity of CeO_2-stabilised tetragonal zirconia polycrystals: I, stress assistance and autocatalysis, J. Am. Ceram. Soc. 71(5) (2010) 343-353. https://doi.org/10.1111/j.1151-2916.1988.tb05052.x.

10. R. Mahendran, S. P. Kumaresh Babu, S. Natarajan, S. Manivannan, A. Vallimanalan, Phase transformation and crystal growth behaviour of 8mol% ($SmO_{1.5}$, $GdO_{1.5}$, and

$YO_{1.5}$) stabilised ZrO_2 powders, Int. J. Miner. Metall. Mater. 24(7) (2017) 842-849. https://doi.org/10.1007/s12613-017-1468-4.

11. G. Chen, Q. N. Li, Y. Q. Ling, H. W. Zheng, J. Chen, Q. Jiang, K. Q. Li, J. H. Peng, M. Omran, L. Gao, Phase stability and microstructure morphology of microwav e-sintered magnesia-partially stabilised zirconia, Ceram. Int. (2020). https://doi.org/10.1016/j.ceramint.2020.09.281.
12. G. Chen, Y.Q. Ling, Q.N. Li, H.W. Zheng, K.Q. Li, Q. Jiang, L. Gao, M. Orman, J.H. Peng, J. Chen, Stability properties and structural characteristics of CaO-partially stabilised zirconia ceramics synthesised from fused ZrO_2 by microwave sintering, Ceram. Int. 46(10) (2020) 16842-16848. https://doi.org/10.1016/j.ceramint.2020.03.261.
13. L.L. Fehrenbacher, L.A. Jacobson, Metallographic observation of the monoclinic-tetragonal phase transformation in ZrO_2, J. Am. Ceram. Soc. 48(3) (2010) 157-161. https://doi.org/10.1111/j.1151-2916.1965.tb16054.x.
14. A. Bogicevic, C. Wolverton, G.M. Crosbie, E.B. Stechel, Defect ordering in aliovalently doped cubic zirconia from first principles. Phys. Rev. B. 64(1) (2001) 014106. https://doi.org/10.1103/PhysRevB.64.014106.
15. S. M. Dezfuli, A. Shanaghi, S. Baghshahi, Effect of Al_2O_3 and Y_2O_3 on the corrosion behaviour of ZrO_2-benzotriazole nanostructured coatings applied on AA2024 via a sol-gel method, Int. J. Miner. Metall. Mater. 25(11) (2018) 1344-1353. https://doi.org/10.1007/s12613-018-1688-2.
16. R.C. Garvie, Structure and thermomechanical properties of partially stabilised zirconia in the CaO-ZrO_2 system, J. Am. Ceram. Soc. 55 (2010) 152-157. https://doi.org/10.1007/978-94-009-0741-6_15.

17. R.H.J. Hannink, P.M. Kelly, B.C. Muddle, Transformation toughening in zirconia-containing ceramics, J. Am. Ceram. Soc. 83(3) (2002) 461-487. https://doi.org/10.1111/j.1151-2916.2000.tb01221.x.

18. S. Fabris, A.T. Paxton, M.W. Finnis, A stabilisation mechanism of zirconia based on oxygen vacancies only. Acta. Mater. 50(20) (2002) 5171-5178. https://doi.org/10.1016/S1359-6454(02)00385-3.

19. M.W. Yan, Y. Li, G.X. Yin, S.H. Tong, J.H. Chen, Synthesis and characterisation of a MgO-$MgAl_2O_4$-ZrO_2, composite with a continuous network microstructure, Ceram. Int. 43(8) (2017) 5914-5919. https://doi.org/10.1016/j.ceramint.2017.01.082.

20. K.Q. Li, J. Chen, J.H. Peng, S. Koppala, M. Omran, G. Chen, One-step preparation of CaO-doped partially stabilised zirconia from fused Zirconia, Ceram. Int. 46(5) (2020) 6484-6490. https://doi.org/10.1016/j.ceramint.2019.11.129.

21. K. Chihwei, Y. Shen, F. Yen, H. Cheng, I. Hung, S. Wen, M. Wang, M. Stack, Phase transformation behaviour of 3mol% yttria partially-stabilised ZrO_2 (3Y-PSZ) precursor powder by an isothermal method, Ceram. Int. 40 (2014) 3243-3251 https://doi.org/10.1016/j.ceramint.2013.09.112.

22. E. Tani, M. Yoshimura, S. Somiya, Revised phase diagram of the system ZrO_2-CeO_2 below 1400 °C, J. Am. Ceram. Soc. 66(7) (2010) 506-510. https://doi.org/10.1111/j.1151-2916.1983.tb10591.x.

23. H. Wang, M.H. Wang, W.Y. Zhang, N. Zhao, W. Wei, Y.H. Sun, Synthesis of dimethyl carbonate from propylene carbonate and methanol using CaO-ZrO_2 solid solutions as highly stable catalysts, Catal. Today. 115(1) (2006) 107-110. https://doi.org/10.1016/j.cattod.2006.02.031.

24. H. Wang. M.H Wang, N. Zhao, W. Wei, Y. Sun, CaO-ZrO_2 solid solution: a highly stable catalyst for the synthesis of dimethyl carbonate from propylene carbonate and

methanol, Catal. Lett. 105(3-4) (2005) 253-257. https://doi.org/10.1007/s10562-005-8699-0.

25. B.T. Lin, M.D. Jean, J.H. Chou, Using response surface methodology for optimizing deposited partially stabilised zirconia in plasma spraying, Appl. Surf. Sci. 253 (2007) 3254-3262. https://doi.org/10.1016/j.apsusc.2006.07.021.
26. M.Y. Zhang, L. Gao, J.X. Kang, J. Pu, J.H. Peng, M. Omran, G. Chen, Stability optimisation of CaO-doped partially stabilised zirconia by microwave sintering, Ceram. Int. 45(17) (2019) 23278-23282. https://doi.org/10.1016/j.ceramint.2019.08.024.
27. K.Q. Li, J. Chen, J.H. Peng, R. Ruan, C. Srinivasakannan, G. Chen, Pilot-scale study on enhanced carbothermal reduction of low-grade pyrolusite using microwave heating, Powder. Technol. 360 (2020) 7523-7530. https://doi.org/10.1016/j.powtec.2019.11.015.
28. G. Chen, K.Q. Li, Q. Jiang, X.P. Li, J.H. Peng, M. Omran, J. Chen, Microstructure and enhanced volume density properties of FeMn78C8.0 alloy prepared via a cleaner microwave sintering approach, J. Clean. Prod. 262 (2020) 121364. https://doi.org/10.1016/j.jclepro.2020.121364.
29. K.Q. Li, G. Chen, J. Chen, J.H. Peng, R. Ruan, C. Srinivasakannan, Microwave pyrolysis of walnut shell for reduction process of low-grade pyrolusite, Bioresource. Technol. 291 (2019) 121838. https://doi.org/10.1016/j.biortech.2019.121838.
30. K. Q. Li, J. Chen, J. H. Peng, R. Ruan, M. Omran, G. Chen, Dielectric properties and thermal behaviour of electrolytic manganese anode mud in microwave field, J. Hazard. Mater. 384 (2019) 121227. https://doi.org/10.1016/j.jhazmat.2019.121227.
31. S.H. Guo, G. Chen, J.H. Peng, J. Chen, J.L. Mao, D.B. Li, L.J. Liu, Preparation of partially stabilised zirconia from fused zirconia using sintering, J. Alloy. Compd. 506(1) (2010) L5-L7. https://doi.org/10.1016/j.jallcom.2010.06.156.

32. S.A. Nightingale, H.K. Worner, D.P. Dunne, Microstructural development during the microwave sintering of yttria-zirconia ceramics, J. Am. Ceram. Soc. 80(2) (1997) 394-400. https://doi.org/10.1111/j.1151-2916.1997.tb02843.x.

33. R. Benavente, M.D. Salvador, F.L. Penaranda-Foix, E. Pallone, A. Borrell, Mechanical properties and microstructural evolution of alumina-zirconia nanocomposites by microwave sintering, Ceram. Int. 40(7) (2014) 11291-11297. https://doi.org/10.1016/j.ceramint.2014.03.153.

34. K.Q. Li, G. Chen, X.T. Li, J.H. Peng, R. Ruan, M. Omran, J. Chen, High-temperature dielectric properties and pyrolysis reduction characteristics of different biomass-pyrolusite mixtures in microwave field, Bioresource. Technol. 294 (2019) 122217. https://doi.org/10.1016/j.biortech.2019.122217.

35. M. Mazaheri, A.M. Zahedi, M.M. Hejazi. Processing of nanocrystalline 8 mol% yttria-stabilised zirconia by conventional, microwave-assisted and two-step sintering, Mat. Sci. Eng. A-struct. 492(1) (2008) 261-267. https://doi.org/10.1016/j.msea.2008.03.023.

36. A. K. Behnami, A. Hoseinpur, M. Sakaki, M. S. Bafghi, K. Yanagisawa, Synthesis of WC powder through microwave heating of WO_3-C mixture, Int. J. Miner. Metall. Mater. 24(2) (2017) 202-207. https://doi.org/10.1007/s12613-017-1396-3.

37. K.Q. Li, J. Chen, J.H. Peng, M. Omran, G. Chen, Efficient improvement for dissociation behaviour and thermal decomposition of manganese ore by microwave calcination, J. Clean. Prod. 260 (2020) 121074. https://doi.org/10.1016/j.jclepro.2020.121074.

38. R.R. Thridandapani, C.E. Folgar, A. Kulp, D.C. Folz, D.E. Clark, Effect of direct microwave sintering on structure and properties of 8 Mol% Y_2O_3-ZrO_2, Int. J. Appl. Ceram. Tec. 8(5) (2011) 1229-1236. https://doi.org/10.1111/j.1744-7402.2010.02570.x.

39. P. Liu, L. B. Zhang, B. G. Liu, G. J. He, J. H. Peng, M. Y. Huang, Determination of dielectric properties of titanium carbide fabricated by microwave synthesis with Ti-

bearing blast furnace slag, Int. J. Miner. Metall. Mater. 28(1) (2021) 88-97. https://doi.org/10.1007/s12613-020-1985-4.

40. Y. Murase, E. Kato, K. Daimon, Stability of ZrO_2 phases in ultrafine ZrO_2-Al_2O_3 mixtures, J. Am. Ceram. Soc. 69(2) (1986) 83-87. https://doi.org/10.1111/j.1151-2916.1986.tb04706.x.

Figure captions

Fig. 1 XRD pattern (a) and Raman spectra (b) of the fused ZrO_2 sample.

Fig. 2 XRD patterns of the MgO-PSZ samples sintered at various temperatures for 1 h.

Fig. 3 XRD patterns of the MgO-PSZ samples sintered at 1200 °C under various durations.

Fig. 4 Raman spectra of the MgO-PSZ samples sintered at various temperatures for 1 h, (a) 900 °C; (b) 1000 °C; (c) 1100 °C; (d) 1200 °C.

Fig. 5 Raman spectra of the MgO-PSZ samples sintered at 1200 °C under various durations, (a) 1 h; (b) 2 h; (c) 3 h; (d) 4 h.

Fig. 6 FT-IR spectra of the MgO-PSZ samples sintered at various temperatures for 1 h, (a) 900 °C; (b) 1000 °C; (c) 1100 °C; (d) 1200 °C.

Fig. 7 FT-IR spectra of the MgO-PSZ samples sintered at 1200 °C under various durations, (a) 1 h; (b) 2 h; (c) 3 h; (d) 4 h.

Fig. 8 SEM images of the MgO-PSZ samples sintered at various temperatures for 1 h, (a)-(b) raw material; (c) 900 °C; (d) 1000 °C; (e) 1100 °C; (f) 1200 °C.

Fig. 9 SEM images of the MgO-PSZ samples sintered at 1200 °C under various durations, (a) 1 h; (b) 2 h; (c) 3 h; (d) 4 h.

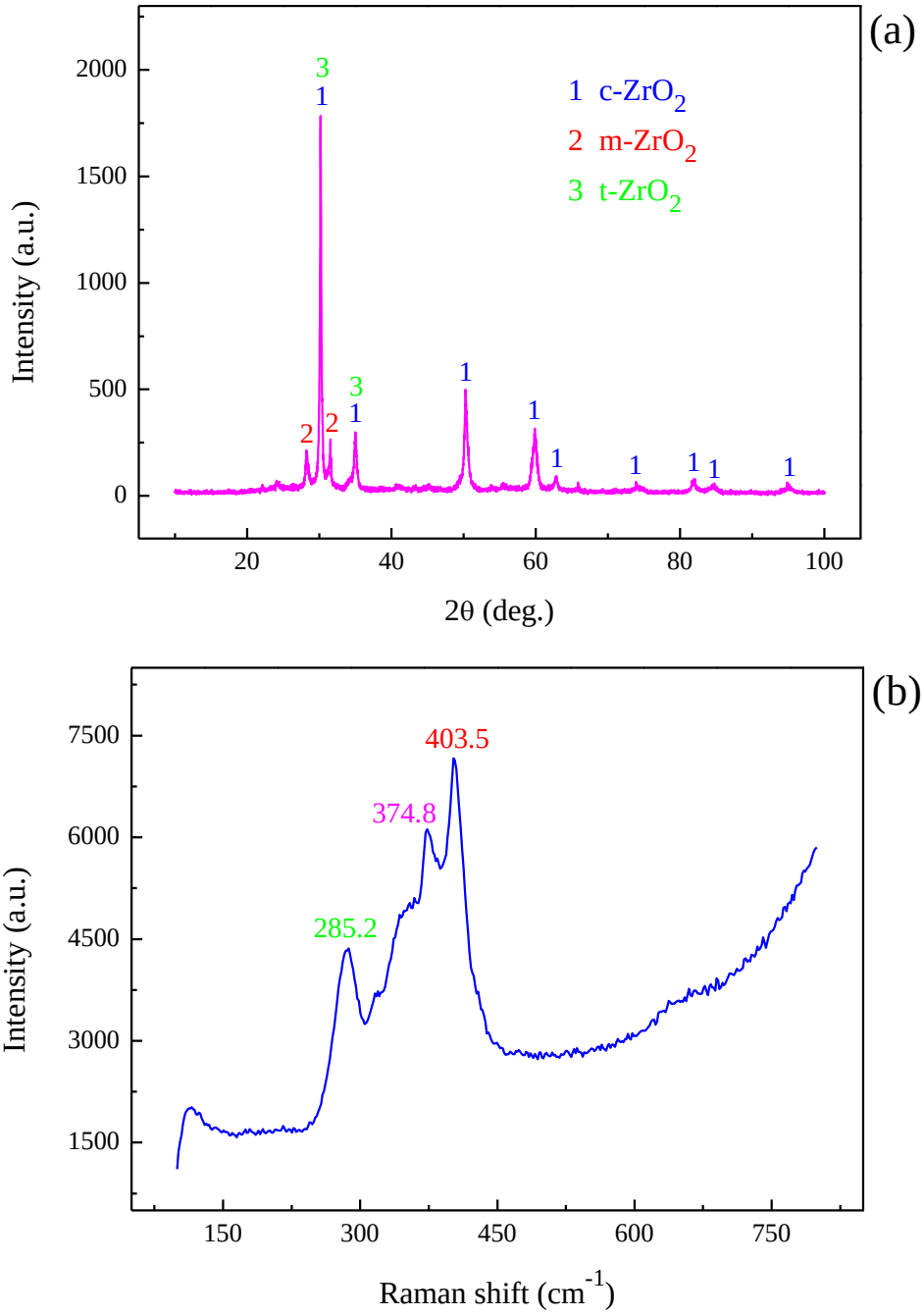

Fig. 1 XRD pattern (a) and Raman spectra (b) of the fused ZrO_2 sample.

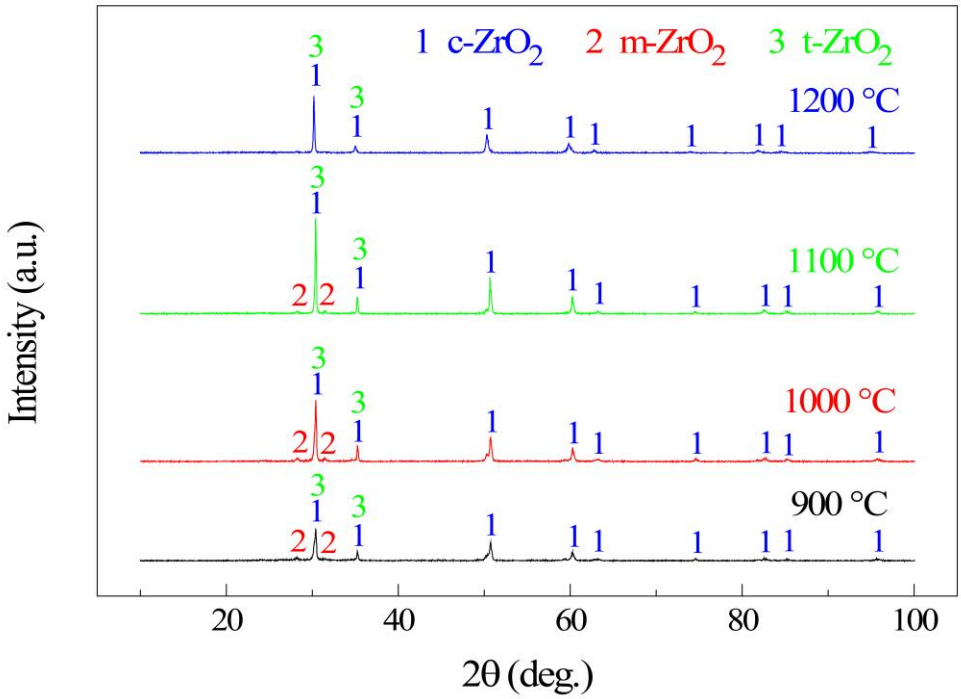

Fig. 2 XRD patterns of the microwave sintered MgO-PSZ samples at various sintering temperatures for 1 h.

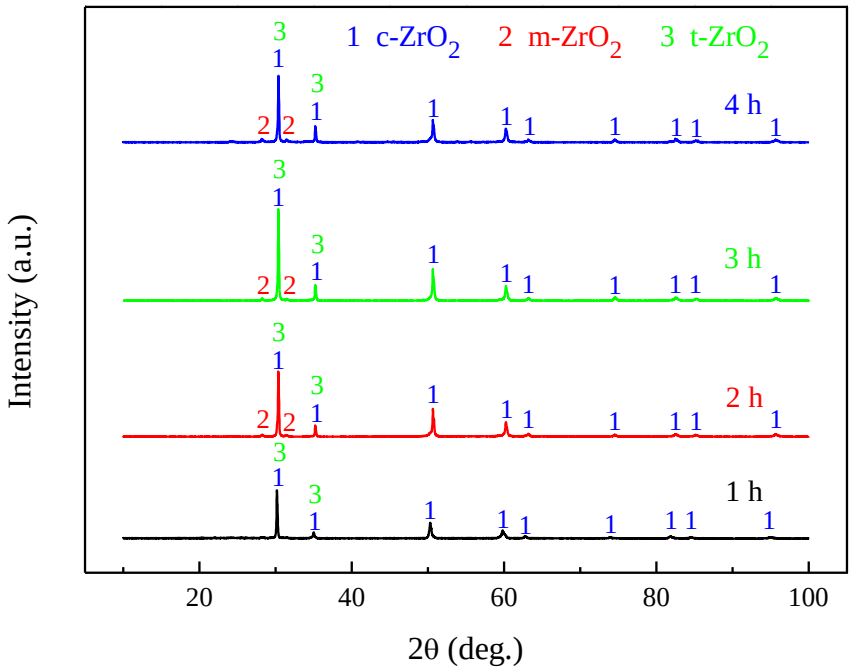

Fig. 3 XRD patterns of the microwave sintered MgO-PSZ samples at 1200 °C under various durations.

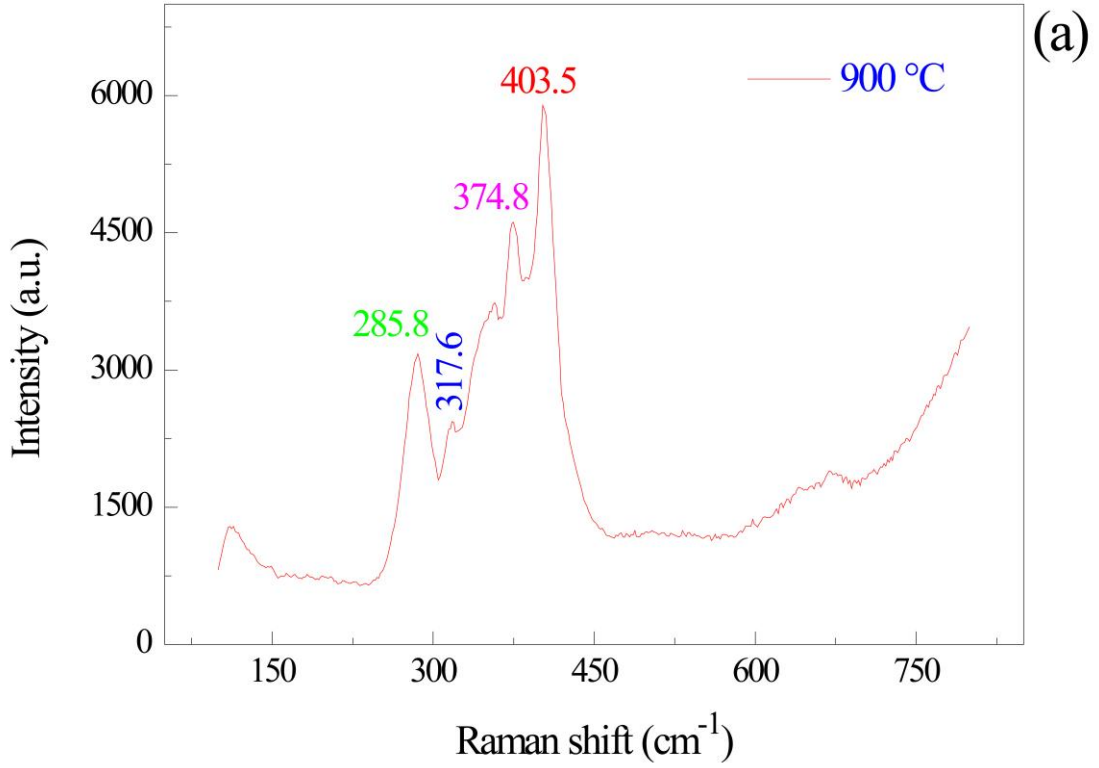
(a)
900 °C
403.5
374.8
285.8
317.6
Intensity (a.u.)
Raman shift (cm-1)
0
1500
3000
4500
6000
150
300
450
600
750

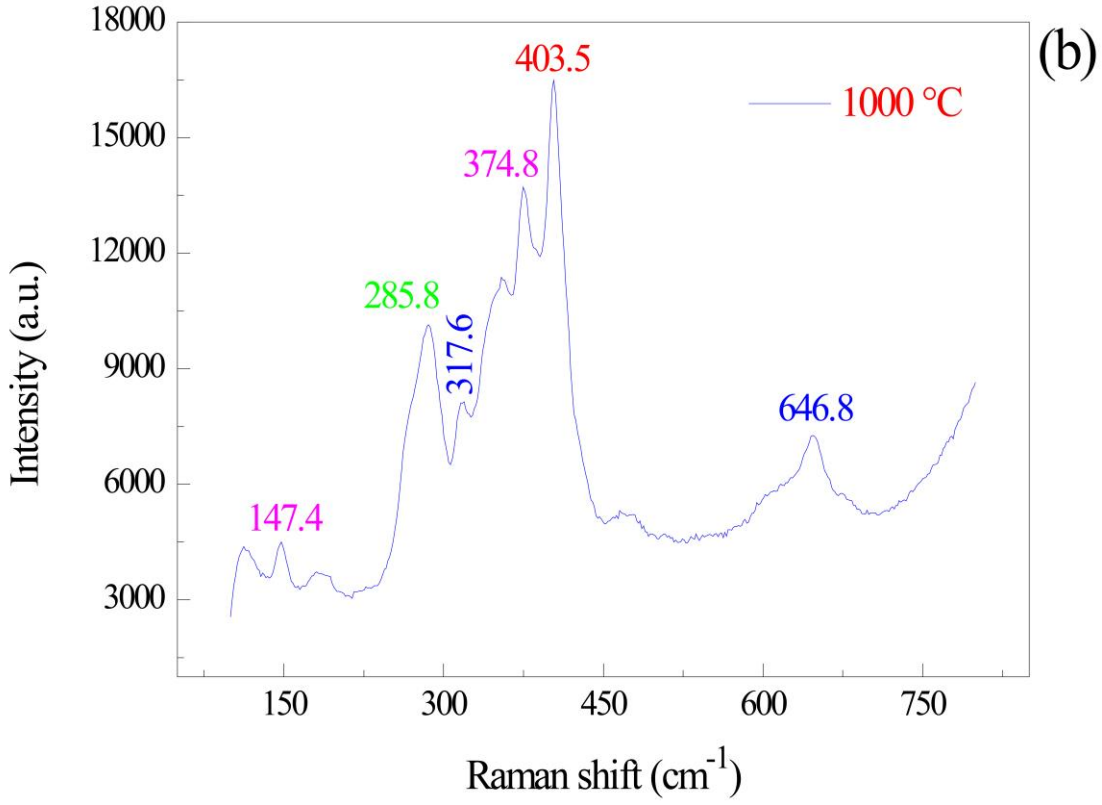
(b)
1000 °C
403.5
374.8
285.8
317.6
646.8
147.4
Intensity (a.u.)
Raman shift (cm-1)
3000
6000
9000
12000
15000
18000
150
300
450
600
750

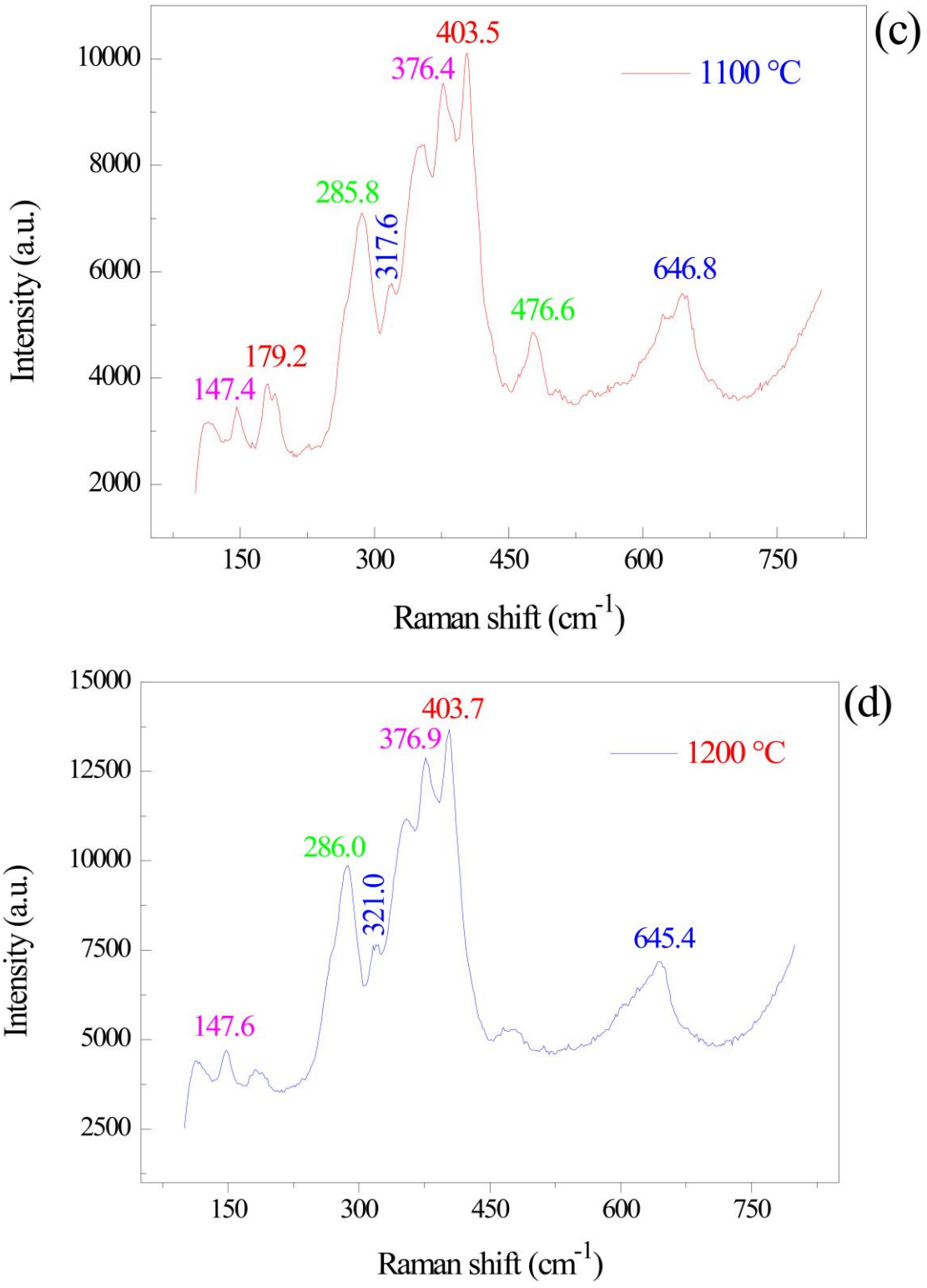

Fig. 4 Raman spectra of the microwave sintered MgO-PSZ samples at various sintering temperatures for 1 h, (a) 900 °C; (b) 1000 °C; (c) 1100 °C; (d) 1200 °C.

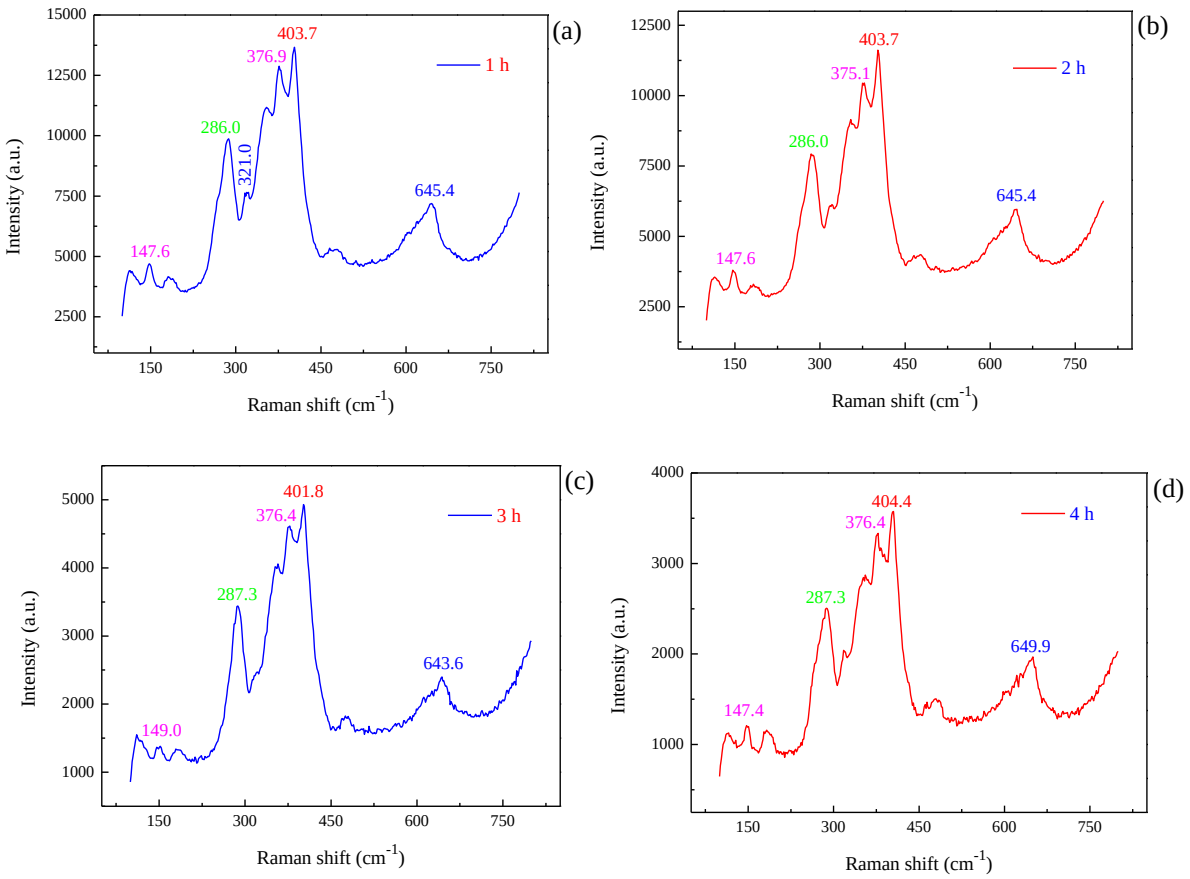

Fig. 5 Raman spectra of the microwave sintered MgO-PSZ samples at 1200 °C under various durations, (a) 1 h; (b) 2 h; (c) 3 h; (d) 4 h.

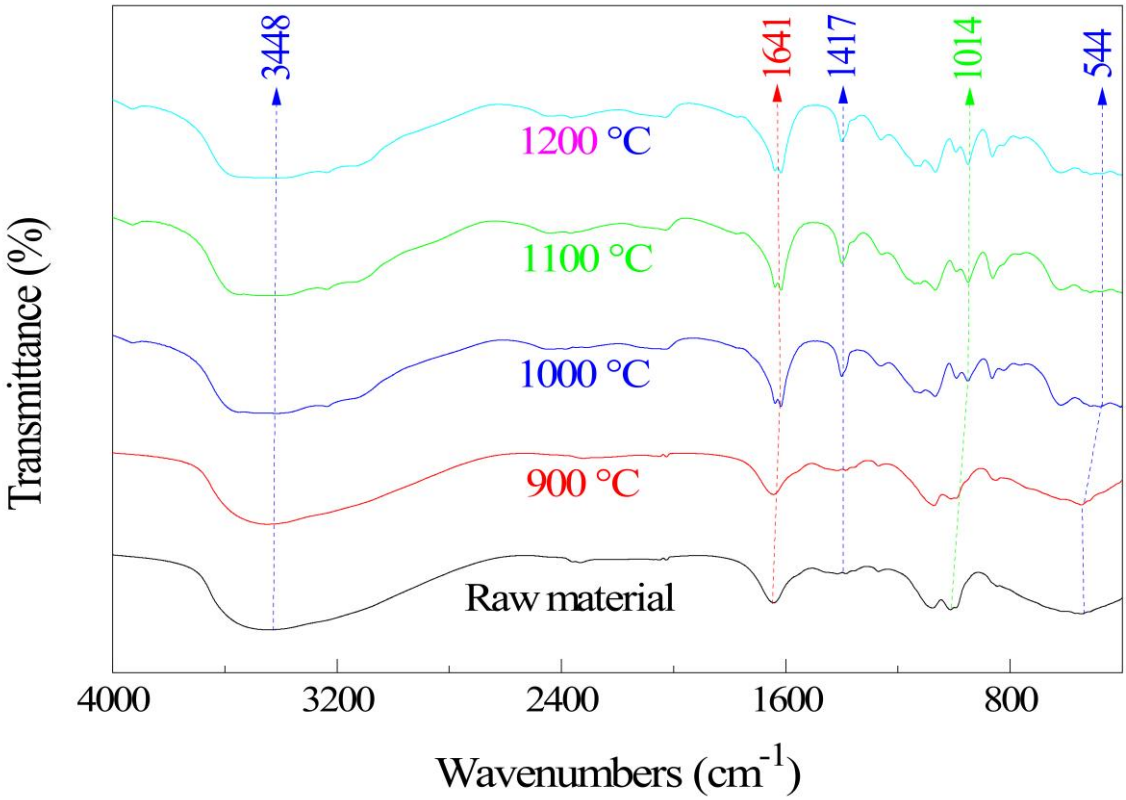

Fig. 6 FT-IR spectra of the microwave sintered MgO-PSZ samples at under various sintering temperatures for 1 h.

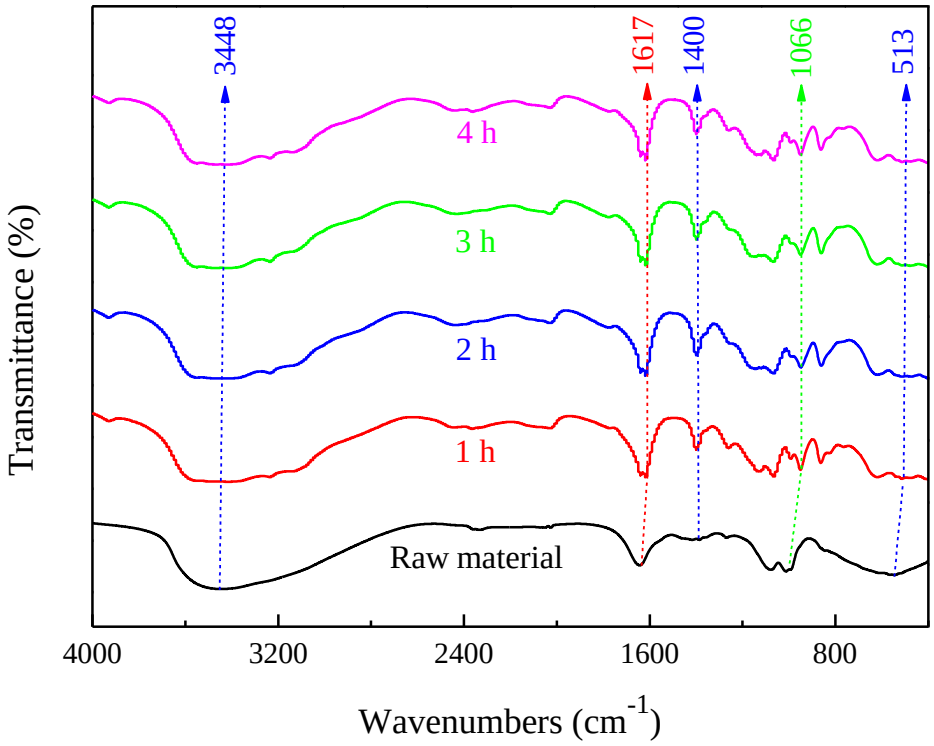

Fig. 7 FT-IR spectra of the microwave sintered MgO-PSZ samples at 1200 °C under various durations.

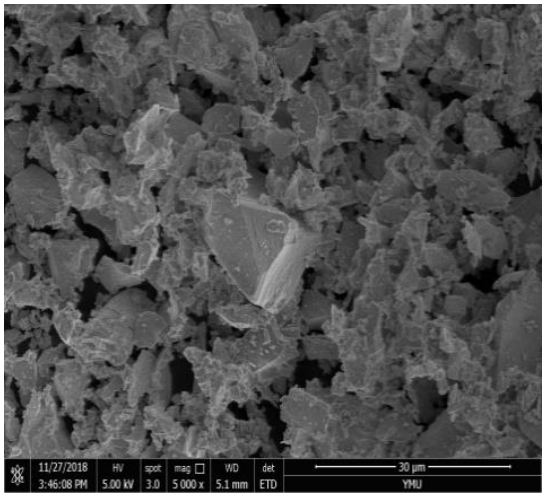
11/27/2018
3:46:08 PM
HV
5.00 kV
spot
3.0
mag
5 000 x
WD
5.1 mm
det
ETD
30 µm
YMU

(a)

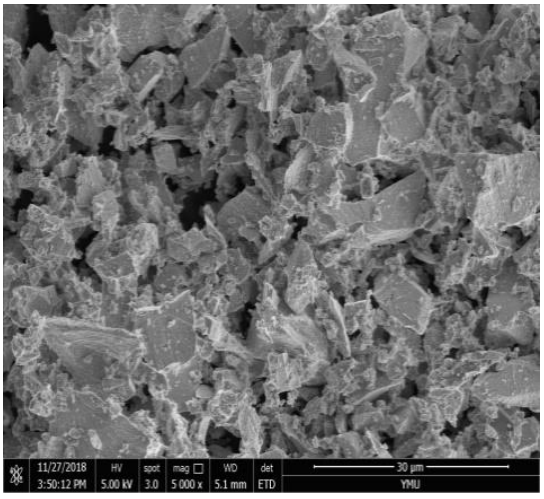
11/27/2018
3:50:12 PM
HV
5.00 kV
spot
3.0
mag
5 000 x
WD
5.1 mm
det
ETD
30 µm
YMU

(b)

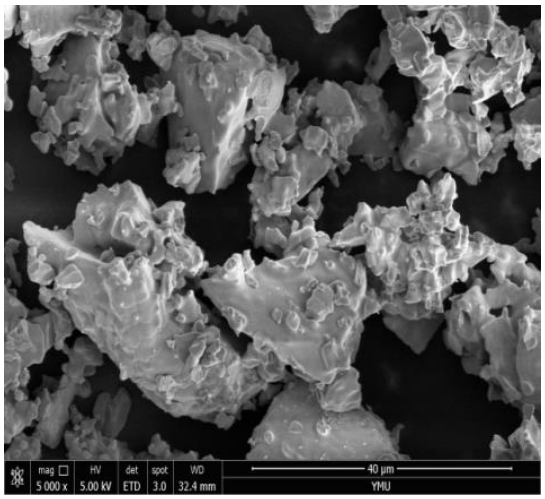
mag
5 000 x
HV
5.00 kV
det
ETD
spot
3.0
WD
32.4 mm
40 µm
YMU

(c)

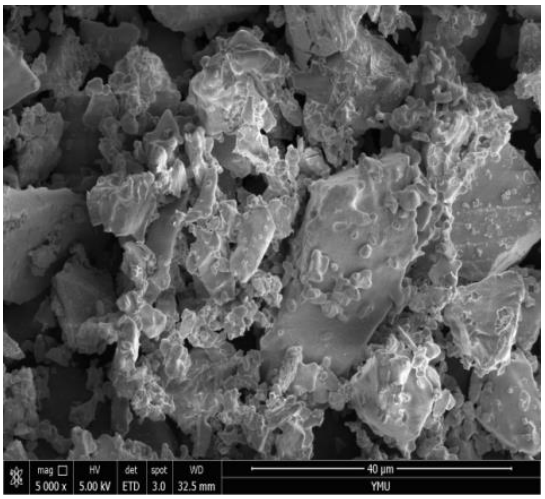
mag
5 000 x
HV
5.00 kV
det
ETD
spot
3.0
WD
32.5 mm
40 µm
YMU

(d)

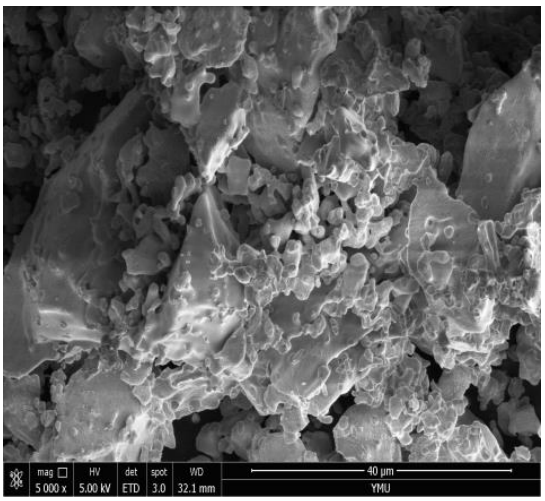
mag
5 000 x
HV
5.00 kV
det
ETD
spot
3.0
WD
32.1 mm
40 µm
YMU

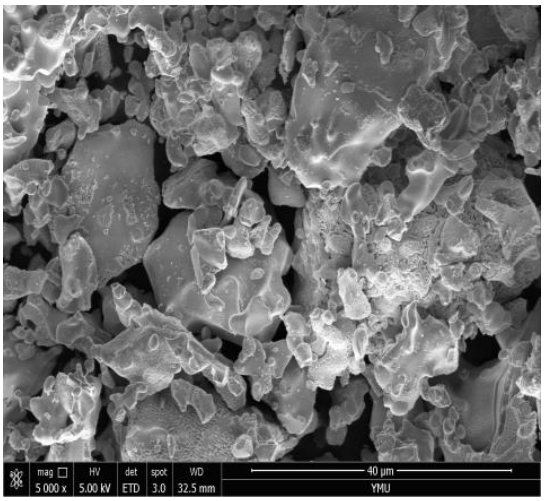
mag
5 000 x
HV
5.00 kV
det
ETD
spot
3.0
WD
32.5 mm
40 µm
YMU

(e) (f)

Fig. 8 SEM images of the microwave sintered MgO-PSZ samples at various sintering temperatures for 1 h, (a)-(b) raw material; (c) 900 °C; (d) 1000 °C; (e) 1100 °C; (f) 1200 °C.

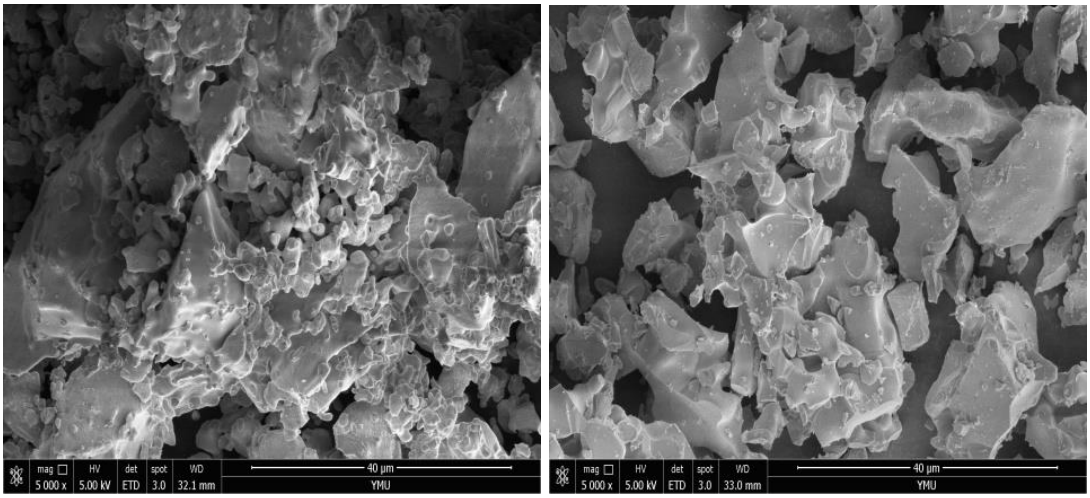

(a) (b)

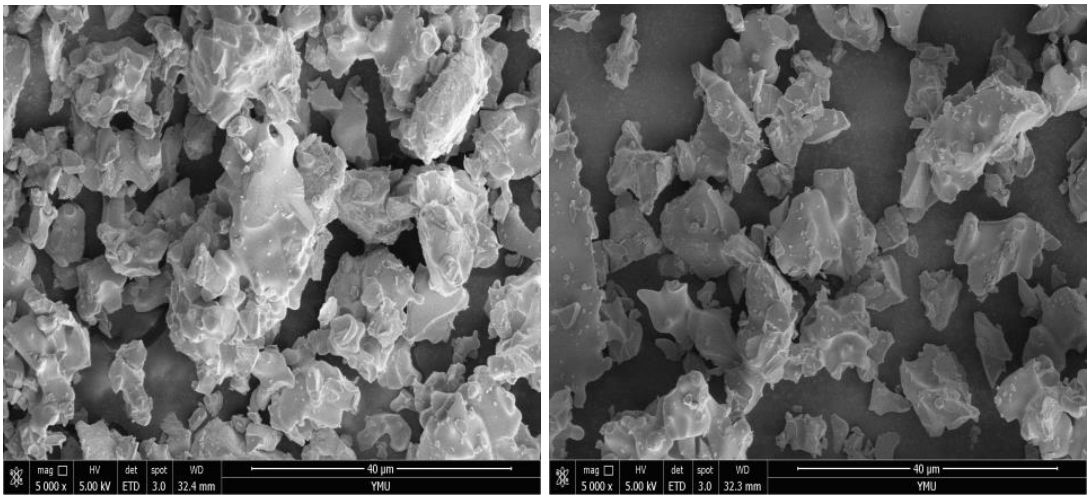

(c) (d)

Fig. 9 SEM images of the microwave sintered MgO-PSZ samples at 1200 °C under various durations, (a) 1 h; (b) 2 h; (c) 3 h; (d) 4 h.

Conflict of interest statement

We declare that we have no financial and personal relationships with other people or organizations that can inappropriately influence our work, there is no professional or other personal interest of any nature or kind in any product, service and/or company that could be construed as influencing the position presented in, or the review of, the manuscript entitled, "*Phase microstructure and morphology evolution of MgO-PSZ ceramics during the microwave sintering process*" by Qiannan Li, Yeqing Ling, Hewen Zheng, Guo Chen, Jin Chen, Sivasankar Koppala, Qi Jiang, Kangqiang Li, Mamdouh Omran and Lei Gao.

Phase microstructure and morphology evolution of MgO-PSZ ceramics during the microwave sintering process

Qiannan Li [a], Yeqing Ling [a], Hewen Zheng [a], Guo Chen [a, **], Jin Chen [a], Sivasankar Koppala [b], Qi Jiang [a], Kangqiang Li [a], Mamdouh Omran [c], Lei Gao [a, *]

[a] *Kunming Key Laboratory of Energy Materials Chemistry, Key Laboratory of Green-Chemistry Materials in University of Yunnan Province, Yunnan Minzu University, Kunming 650500, P.R. China.*

[b] *Panjin Institute of Industrial Technology, Dalian University of Technology, Panjin 124221, Liaoning, P.R. China.*

[c] *Process Metallurgy Research Group, Faculty of Technology, University of Oulu, Finland.*

[*] Corresponding author: glkust2013@hotmail.com

[**] Co-corresponding author: guochen@kust.edu.cn

Abstract:

In the present study, controllable microwave sintering was applied to prepare partially stabilised zirconia ceramics with enhanced phase composition and a more uniform structure. To reveal the phase interface properties and structural changes of PSZ ceramics during the microwave sintering process, XRD, FT-IR, Raman, and SEM characterisations were utilised. XRD analysis and Raman analysis demonstrated that the increase of sintering temperature promoted the martensite conversion. However, prolonging duration time was unconducive to the retention of the stable phase. Additionally, the FT-IR characteristic peak movement caused by the reversible phase martensite transformation was observed. Furthermore, SEM analysis found that microwave treatment improved the grain size and structure distribution of the as-received MgO-PSZ sample. This work constructed a controllable technical prototype of preparing PSZ ceramics via microwave sintering, which can provide a theoretical basis and experimental basis for further industrial production.

Keywords: MgO-PSZ ceramics; microwave sintering; phase microstructure; surface morphology

1 Introduction

Zirconia (ZrO_2) has widely been applied as ceramic coatings, high-temperature parts, and structural ceramic materials, etc., which is attributed to its distinct physical-chemical performances including low thermal conductivity, high hardness, high thermal stability, and high melting point [1-4]. During the phase change process of ZrO_2 where the lattice of ZrO_2 material is modified without the composition variation, the conversion between monoclinic

phase (m-ZrO_2) and tetragonal phase (t-ZrO_2) is reversible. Therefore, the phase change of ZrO_2 is considered as martensite transformation [5-8]. However, pure ZrO_2 material presents a volume change effect in the reversible martensite transformation process between the monoclinic phase and tetragonal crystals [9-11]. The volume change effect is mainly manifested by the 5% volume expansion in the cooling process and the 3.25% volume shrinkage in the heating process, resulting in the accumulation of tensile stress inside pure ZrO_2 material and further cause the cracking of its products, which seriously limits the application of pure ZrO_2 materials [12-13]. Therefore, pure ZrO_2 needs to be stabilised to achieve a toughening effect.

Currently, the toughening effect of ZrO_2 materials is mainly achieved through doping stabilisers [14-15]. By adding the appropriate stabiliser, the phase transition temperatures of the monoclinic crystal (m) into tetragonal crystal (t) and tetragonal crystal (t) into cubic crystal (c) can be reduced. Meanwhile, cubic and tetragonal crystals that exist stably under high temperature can also be stable or meta-stable at room temperature. The crystalline stability of the ZrO_2 materials doped with stabiliser produces the phase change of tetragonal into the monoclinic crystal, induced by stress when bearing [16]. Attributed to the volume effect produced by the phase transition of t-ZrO_2→m-ZrO_2, a lot of fracture energy is absorbed. The material exhibits abnormally high fracture toughness, rendering the doped ZrO_2 materials toughen with high toughness and high wear resistance characteristics [17]. Commonly, the doped stabilisers are mainly alkaline-earth and rare earth oxides. Meanwhile, the difference in radius between the oxides' ionic and Zr^{4+} should be less than 40% [18]. Notably, MgO [19], CaO [20], Y_2O_3 [21] and CeO_2 [22] are more commonly used. The

stability mechanism is generally explained as: the cations of stabilisers such as Mg^{2+}, Ca^{2+}, Ce^{4+}, and Y^{3+} have certain solubility in ZrO_2 material. Therefore, those cations can replace Zr^{4+} and form a solid replacement solution, which hinders the transition of tetragonal crystal to monoclinic crystal, reducing the transition temperature of tetragonal crystal into the monoclinic crystal and making tetragonal crystal metastable to room temperature [23-24]. Through controlling the type, amount or grain size of the doped stabiliser, ZrO_2 material with different forms of stable state can be obtained, and it is generally divided into three kinds: tetragonal zirconia polycrystalline (TZP), full stabilised zirconia (FSZ), and partially stabilised zirconia (PSZ) [25-26]. PSZ materials contain a phase-changeable tetragonal phase, which is commonly used as phase change toughening ceramic materials. At present, the preparation of PSZ ceramics mainly adopts the electric heating method. However, due to the problems of high temperature (above 1450 °C), long operation time, and serious heat loss during the heating process, the sintering performance of PSZ ceramics prepared is unstable, limiting the development and application of PSZ ceramics materials [16]. Therefore, new methods for preparing PSZ ceramics are urgently needed to be explored, expecting to realise the control of the performance of PSZ ceramics.

Microwave heating technology has become a burgeoning technical means for quickly preparing high-performance new materials and modifying conventional materials, based on the special energy transfer and conversion mechanism, as well as rapid heating and selective heating characteristics [27-30]. Guo et al. [31] explored the microwave heating characteristics of fused ZrO_2. They reported that fused ZrO_2 was heated to 1475 °C within 4 min. The finding denotes the feasibility of applying microwave heating means on ZrO_2 ceramics

preparation. Nightingale et al. [32] investigated the microstructure change of Y_2O_3-doped ZrO_2 ceramics. They highlighted that the microwave sintered sample had more dense microstructures compared to conventionally heated samples. Benavente et al. [33] utilised microwave sintering means to synthesise Al_2O_3-ZrO_2 nanocomposites. The study results indicated that in comparison to conventional heating, higher Young′s modulus, density, and hardness, homogeneous microstructure, and excellent fracture toughness properties were obtained. Microwave heating is different from the heat conduction process of conventional heating, with high heating efficiency; therefore, applying microwave heating as an alternative means of conventional heating has significant advantages in energy saving and emission reduction for the transformation of high energy-consuming industries [34-36]. Meanwhile, microwave heating can improve the uniformity and yield of products and optimise the microstructure and performance of the processed materials [37-39].

In this work, focusing on the key issues in the efficient utilisation and quality improvement of ZrO_2 material, the special energy transfer and energy conversion method of microwave sintering means were fully used to prepare PSZ ceramics, using fused ZrO_2 as the research object and magnesium oxide (MgO) as the stabiliser, aiming to solve the technical problems of low product quality controllability, high process temperature and long operation time during the conventional preparation process of PSZ ceramics. Meanwhile, the transformation and evolution of the components of the multi-phase complex system in fused ZrO_2 under microwave action were studied. The influences of sintering temperature and duration time on the phase interface properties and structural changes of MgO-doped PSZ ceramics were discussed.

2 Materials and methods

2.1 Materials

The ZrO_2 raw material was sourced from a factory in Zhengzhou City, Henan Province, China. The chemical component analysis of the fused ZrO_2 sample was detailed as follows (%/(w/w): ZrO_2, 92.4; MgO, 4.0; SiO_2, 2.3; Al_2O_3, 1.0; TiO_2, 0.2; Fe_2O_3, 0.1, respectively. It was extracted that the main components of the fused ZrO_2 sample were ZrO_2 and MgO phases, wherein the MgO phase was the doped stabiliser. Additionally, Fig. 1 illustrated the Raman spectra and XRD pattern of the fused ZrO_2 sample. As presented in Fig. 1(a), it was determined that in the fused ZrO_2 sample, cubic crystal (JCPDS: 49-1642) and monoclinic crystal (JCPDS: 37-1484) undoubtedly existed, but there was an absence of the diffraction peak of MgO phase detected, signifying that the stable replacement solid solution structure was formed, with MgO stabiliser entering the lattice node of ZrO_2. Moreover, tetragonal crystal (JCPDS: 42-1164) and cubic crystal overlapped at the diffraction peaks of 2θ=30.18 °and 2θ=35.15 °. Therefore, it can be confirmed that in the MgO-doped ZrO_2 sample, there contained a cubic phase and a monoclinic phase of ZrO_2. However, the tetragonal phase of ZrO_2 cannot be determined, which needed another analysis method like Raman characterisation to test. Besides, from the Raman spectra of the fused ZrO_2 sample (Fig. 1(b)), three characteristic peaks caused by the Raman vibration arose at 285.2 cm^{-1}, 374.8 cm^{-1}, and 403.5 cm^{-1}, respectively. Among the three characteristic peaks, the peaks at 374.8 cm^{-1} and 403.5 cm^{-1} were due to m-ZrO_2 phases' B_g vibration, the peak at 285.2 cm^{-1} was caused by tetragonal crystals' E_g vibration, denoting that minority tetragonal crystal

existed in the raw material. In summary, the fused ZrO_2 sample can be classified as Partially Stabilised Zirconia (PSZ), with MgO doped as the stabiliser, which is also named magnesium oxide-doped partially stabilised zirconia (MgO-PSZ) ceramics material.

2.2 Instrumentation

The sintering experiments for the fused ZrO_2 materials were furnished in the high-temperature microwave box reactor (RWS-6, Hunan Thersun Thermal Energy Technology Co., Ltd.). The microwave reactor mainly included a microwave oven cavity, microwave energy feeding system, cooling water machine, thermal insulation system, air extraction system, intelligent control system, infrared thermometer, and other auxiliary equipment.

2.3 Characterisation

The change in phase, surface morphology, and microstructure of magnesia-doped PSZ ceramics during the microwave sintering process were explored through the comparison between the raw ZrO_2 samples with and without sintering treatment by microwaves, using XRD, Raman, FT-IR, and SEM characterisations. Wherein the X-ray diffractometer (D8 ADVANCE A25×, Bruker, Germany) was utilised to characterise the phase evolution of MgO-PSZ samples, with Cu target Ka-ray (λ=1.54056 Å) as the target source; the Confocal Raman spectrometer (InVia, Renishaw, UK) was used to perform the chemical structures of MgO-PSZ samples, scattering between the spectral detection area of 100 cm^{-1}-800 cm^{-1}; the Fourier infrared spectrometer (NICOLET-IS10, American) was responsible for determining the surface functional groups of MgO-PSZ samples, attaching the scanning spectral regime of 4000 cm^{-1}-500 cm^{-1}; also, the scanning electron microscope (XL30ESEM-TM, Philips, Netherlands) was utilised to observe the microstructures of MgO-PSZ samples.

2.4 Procedure

The raw MgO-PSZ material was firstly dried under 105 °C by a drying oven (FX101-1) lasting for 12 h. Then, the dried raw material was sampled using an electronic balance (AL-104) with a mass of 50.0 g, followed by the weighted sample was transformed into the high-temperature microwave box reactor. The sintering experimental parameters were detailed as follows: sintering temperature was adjustable among 900 °C, 1000 °C, 1100 °C, and 1200 °C, duration time was adjustable among 1 h, 2 h, 3 h, and 4 h, and microwave heating power was maintained at 3 kW. Once the sintering experimental parameters reached the set values, the high-temperature microwave box reactor stopped working. The sintered samples were naturally cooled in the microwave reactor and collected for characterisation analysis.

3 Results and discussion

Sintering temperature and duration time present great influences on the performance and microstructure of MgO-doped PSZ ceramics samples. Through adjusting sintering temperature and duration time, the phase microstructure and morphology evolution of MgO-doped PSZ ceramics during the microwave sintering process were unveiled using XRD, Raman, FT-IR, and SEM characterisations, further contribute to determining the technological conditions of the microwave sintering approach.

3.1 XRD characterisation

3.1.1 Influence of sintering temperature

The XRD patterns of the synthesised MgO-PSZ samples under various microwave sintering temperatures were depicted in Fig. 2, wherein the duration time was constant at 1 h.

As illustrated in Fig. 2, under microwave processing at 900 °C for 1 h, the main phases in the sintered sample were strong monoclinic and cubic crystals. The diffraction peaks at 2θ=30.12°, 2θ=50.22°, and 2θ=34.96° belonged to cubic crystal. The diffraction peaks exactly corresponded to the (111), (200) and (220) three strong crystal planes of c-ZrO_2 phase; and m-ZrO_2 phases' diffraction peaks emerged at 2θ=28.06° and 2θ=31.24°. In contrast to the raw material, the diffraction peaks of the MgO-PSZ sample sintered at 900 °C were absent of obvious refinement, with small miscellaneous peaks. This finding manifested that under this experimental condition (at 900 °C for 1 h), the sample crystal structure was defective. The crystal structure of some samples was still in the amorphous phase, accompanied by the phase change reaction had not started in the sample. As temperature lifted to 1000 °C, the peak intensity at 2θ=30.12° belonging to cubic crystal was significantly enhanced. Meanwhile, m-ZrO_2 phase diffraction peaks' intensities at 2θ=28.06° and 2θ=31.24° were also enhanced. The two diffraction peaks exactly corresponded to the (111) crystal plane of the c-ZrO_2 phase. Compared to the MgO-PSZ sample sintered at 900 °C, the intensities of each characteristic peak became larger. The peak shape was refined, indicating that the grains had better development under 1000 °C.

With the temperature rising to 1100 °C, c-ZrO_2 phases' peak intensities continued to increase, and m-ZrO_2 phases' peak intensities gradually decreased, as presented in Fig. 2. The diffraction peaks of the stable phase gradually refined with temperature improving, indicating that the transformation of m-ZrO_2 into t-ZrO_2 began. As temperature improved to 1200 °C, the m-ZrO_2 phase disappeared, indicating that increasing sintering temperature promoted the added magnesium ions gradually entered the ZrO_2 lattice and acted on the magnesium ions

(Mg^{2+}) [14, 18]. Meanwhile m-ZrO_2 phase was transformed into the t-ZrO_2 phase and kept it to room temperature, further to render the gradual decrease of the content of m-ZrO_2 phase. Also, the m-ZrO_2 phases' diffraction peak disappeared at 1200 °C, as shown in Fig. 2. According to the calculation formula of the stability rate of ZrO_2 ceramics material [40], the stability rate obtained under a temperature of 1200 °C was highest among those sintering temperatures. Hence, the favourable sintering temperature could be considered at 1200 °C.

3.1.2 Influence of duration time

Maintaining the sintering temperature constant at 1200 °C and controlling duration time among the regime of 1 h~4 h, influences of duration time on the phase change were explored, and the results were depicted in Fig. 3. As shown in Fig. 3, after sintering treatment at 1200 °C for 1 h, the diffraction peaks of the three strong (111), (200) and (220) crystal planes of c-ZrO_2 phase arose at 2θ=30.12°, 2θ=50.220° and 2θ=34.960°, meanwhile the intensities of the diffraction peaks were very high. In contrast to the raw ZrO_2 sample, monoclinic crystal vanished, denoting that the phase conversion of the ZrO_2 sample was complete under those conditions, with a large amount of monoclinic crystal converted to tetragonal crystal, and the grains of the c-ZrO_2 phase gradually grew. As duration time prolonged to 2 h, c-ZrO_2 phases' diffraction peak intensity in the sample significantly enhanced. However, the m-ZrO_2 phase diffraction peaks appeared at 2θ=28.06° and 2θ=31.24°. The experimental phenomenon indicated that prolonging duration time promoted the growth of the grains of the c-ZrO_2 phase and the reversible transformation between t-ZrO_2 and m-ZrO_2 phases.

As duration time prolonged to 3 h, the peak intensity belonging to the (111) crystal plane of c-ZrO_2 phase significantly increased; in contrast, m-ZrO_2 phases' peak intensities at

2θ=28.06° and 2θ=31.24° did not change much, indicating that c-ZrO_2 phase grains grew well with the extension of duration time. With duration time continually improving to 4 h, c-ZrO_2 phases' peak intensities had weakened, especially the XRD diffraction peaks located at 2θ=30.12°, 2θ=50.22°, and 2θ=34.96°. Furthermore, the intensity of the m-ZrO_2 phase diffraction peak became enhanced, compared to the MgO-doped PSZ sample synthesised under a duration time of 3 h. Therefore, it can be summed that the extension of duration time was unconducive to the retention of the stable phase, and the favourable duration time could be considered at 1 h.

3.2 Raman characterisation

3.2.1 Influence of sintering temperature

Controlling the duration time constant at 1 h and varying sintering temperature among 900 °C to 1200 °C, influences of sintering temperature on the chemical structure were explored, and the obtained Raman spectra were plotted in Fig. 4. As illustrated in Fig. 4(a), the Raman spectra of the sample were synthesised at 900 °C and the Raman spectra of the sample showed the strongest peak at 403.5 cm^{-1}, the second strongest peaks appeared at 285.8 cm^{-1} and 374.8 cm^{-1}, and a medium intensity peak at 317.6 cm^{-1}. The Raman vibration characteristic peaks at 285.8 cm^{-1} and 317.6 cm^{-1} belonged to the t-ZrO_2 phase. The Raman peaks located at 374.8 cm^{-1} and 403.5 cm^{-1} belonged to the m-ZrO_2 phase. Besides, as presented in Fig. 4(a), the Raman activity of monoclinic crystal and tetragonal crystal appeared. Meanwhile, the corresponding XRD pattern (Fig. 2) denoted that there was an amorphous phase at this temperature (900 °C), indicating that there was relatively minority tetragonal crystal. Moreover, in contrast to the raw ZrO_2 sample, the peak intensities of the

two phases were not very high, indicating that the transformation of monoclinic crystal into tetragonal crystal was not intense under the temperature of 900 °C. With the temperature increasing to 1000 °C, six Raman vibration characteristic peaks appeared in the Raman spectrum of the MgO-PSZ sample, located at 648.8 cm^{-1}, 403.5 cm^{-1}, 374.8 cm^{-1}, 317.6 cm^{-1}, 285.8 cm^{-1}, and 147.4 cm^{-1}, respectively, as depicted in Fig. 4(b). Wherein the Raman peaks caused by the B_g and E_g Raman vibrations of tetragonal crystal located at 317.6 cm^{-1}, 147.4 cm^{-1}, 285.8 cm^{-1}, and 646.8 cm^{-1}; and the Raman peak at 403.5 cm^{-1} resulted in the B_g Raman vibration of the monoclinic crystal. Compared with the MgO-doped PSZ sample synthesised at 900 °C, the relative intensities of the Raman vibration characteristic peak in the MgO-PSZ sample sintered at 1000 °C significantly enhanced and became sharp, indicating that the conversion of monoclinic crystal into tetragonal crystal started, further to cause the content of tetragonal crystal increased.

As the temperature rose to 1100 °C, eight Raman vibration characteristic peaks appeared, as presented in Fig. 4(c). The four peaks at 317.6 cm^{-1}, 147.4 cm^{-1}, 285.8 cm^{-1}, and 646.8 cm^{-1} were assigned to tetragonal crystals' B_g and E_g Raman vibrations. The Raman peak at 403.5 cm^{-1} resulted in the B_g Raman vibration of the monoclinic crystal. At this temperature, the Raman vibration modes of the t-ZrO_2 phase were more obvious, but the m-ZrO_2 phase' peak intensity was weakened at 403.5 cm^{-1}, indicating that the content of the m-ZrO_2 phase had decreased. The phenomenon denoted that a certain amount of the stable phase in the sample was stored till room temperature, and it did not transform into the m-ZrO_2 phase. With temperature continually lifting to 1200 °C, the strongest peak arose at 403.7 cm^{-1}, the secondary strongest peaks appeared at 286.0 cm^{-1} and 376.9 cm^{-1}, and the moderate-intensity

peaks arose at 147.6 cm^{-1}, 321.0 cm^{-1}, and 645.4 cm^{-1}, as illustrated in Fig. 4(d). In contrast to the MgO-doped PSZ sample synthesised at 1100 °C (Fig. 4(c)), the intensities of the Raman peaks at 286.0 cm^{-1} and 321.0 cm^{-1} belonging to tetragonal crystal enhanced with the temperature rising. Meanwhile, some characteristic peaks disappeared, signifying that the increase in temperature contributed to the phase transition of monoclinic crystal into the tetragonal crystal, further reducing the monoclinic crystal phase. The conclusions concluded from the Raman spectra analysis corresponded to the XRD pattern (Fig. 2).

3.2.2 Influence of duration time

Maintaining temperature constant at 1200 °C and varying duration time from 1 h to 4 h, influences of duration time on the chemical structure were probed, and the Raman spectra were depicted in Fig. 5. After sintering at 1200 °C lasting for 1 h, six Raman activities were detected in the Raman spectrum of the sample, located at 403.7 cm^{-1}, 286.0 cm^{-1}, 376.9 cm^{-1}, 147.6 cm^{-1}, 321.0 cm^{-1}, and 645.4 cm^{-1}, as presented in Fig. 5(a). The characteristic peaks caused by the B_g and E_g Raman vibrations of the t-ZrO_2 phase are 147.6 cm^{-1}, 286.0 cm^{-1}, 321.0 cm^{-1}, and 645.4 cm^{-1}, the characteristic peaks assigned to the B_g Raman vibration of m-ZrO_2 phase are 376.9 cm^{-1} and 403.7 cm^{-1}. Referring to the raw ZrO_2 material, the m-ZrO_2 phase's content in the MgO-PSZ sample under 1200 °C decreased, which was attributed to the convection of a large amount of m-ZrO_2 phase into the t-ZrO_2 phase. With duration time prolonging to 2 h, the strongest peak arose at 403.7 cm^{-1}, and other strong peaks arose at 286.0 cm^{-1}, 375.1 cm^{-1}, 147.6 cm^{-1}, and 645.4 cm^{-1}, as displayed in Fig. 5(b). By comparison with Fig. 5(a), it was observed that with the extension of a duration time, the relative

intensities of the peaks including 147.6 cm^{-1}, 286.0 cm^{-1}, and 645.4 cm^{-1} decreased, indicating the content of the t-ZrO_2 phase decreased.

As duration time extended to 3 h, the Raman peaks including 149.0 cm^{-1}, 287.3 cm^{-1}, and 643.6 cm^{-1} were attributed to t-ZrO_2 phases' Raman vibration, and the Raman peaks at 376.4 cm^{-1} and 401.8 cm^{-1} were caused by m-ZrO_2 phases' Raman vibration. Under the conditions of the holding time of 3 h, t-ZrO_2 phases' characteristic peaks intensities were significantly weakened compared with Fig. 5(b), denoting t-ZrO_2 phase content decreased with the extension of duration time. Meanwhile, the peak frequencies of the Raman vibration peaks at 149.0 cm^{-1}, and 287.3 cm^{-1} shifted to a high wave number, resulting in a blue shift. As duration time prolonged to 4 h, the Raman spectrum of the sintered MgO-PSZ sample showed five Raman active vibrations, as presented in Fig. 5(d). Referring to Fig. 5(c), the Raman activities in the sample were the same, only the position of the Raman peaks had changed slightly. The Raman vibration characteristic peaks of the t-ZrO_2 phase continued to weaken, only reaching about 4500 (a.u.). The Raman spectra analysis indicated that extending duration time was conductive to the phase transition of monoclinic crystal into the tetragonal crystal, further to render tetragonal crystal decreased. The findings obtained from Raman spectra also matched the XRD pattern (Fig. 3).

3.3 FT-IR characterisation

3.3.1 Influence of sintering temperature

Maintaining duration time constant at 1 h and controlling sintering temperature regime of 900 °C~1200 °C, effects of sintering temperature on the microscopic surface functional groups of the magnesia-doped PSZ samples were investigated, and the FT-IR spectra were

plotted in Fig. 6. As displayed in Fig. 6, five FT-IR characteristic peaks were detected in the raw fused ZrO_2 sample, including 3447.56 cm^{-1}, 1643.53 cm^{-1}, 1416.46 cm^{-1}, 1013.39 cm^{-1} and 545.50 cm^{-1}. Specifically, the FT-IR peak at 545.50 cm^{-1} resulted in the Zr-O bonds' contraction vibration; the characteristic peak at 1013.39 cm^{-1} was due to the O-H bonds' bending vibration; the FT-IR peak at 1416.46 cm^{-1} was assigned to the sample adsorbs carbon dioxide (CO_2) in the air; the characteristic peaks at 1643.53 cm^{-1} were attributed to H-O-H bonds' bending vibration. The H-O-H bonds were generated by the sample absorbs water molecules in the air; and the FT-IR peak at 3447.56 cm^{-1} resulted in the O-H bonds' contraction vibration.

After sintering at 900 °C for 1h, the infrared spectroscopy peaks at 546.14 cm^{-1}, 1011.31 cm^{-1}, 1416.97 cm^{-1}, 1641.25 cm^{-1}, and 3448.15 cm^{-1} appeared in the sintered MgO-PSZ sample. Compared with the raw ZrO_2 sample, the wavenumbers of the five FT-IR peaks hardly changed. With temperature rising to 1000 °C, the five FT-IR peaks arose, including 3448.67 cm^{-1}, 1617.52 cm^{-1}, 1400.66 cm^{-1}, 1068.09 cm^{-1}, and 477.95 cm^{-1}, respectively. Besides, the FT-IR peak at 477.95 cm^{-1} was assigned to the stretching vibration of the Zr-O bonds, which is the FT-IR peak of the t-ZrO_2 phase; meanwhile, by the comparison between the raw material and the MgO-PSZ sample sintered at 900 °C, it can be concluded that the characteristic peak frequency shifted to a low wavenumber, resulting in a red shift. Notably, the red shift was induced by that monoclinic phase that started to convert into a tetragonal phase with a temperature rising. As temperature improved to 1100 °C, the five FT-IR peaks arose at 3448.83 cm^{-1}, 1617.32 cm^{-1}, 1416.27 cm^{-1}, 1067.04 cm^{-1}, and 514.36 cm^{-1}, respectively. Referring to the MgO-PSZ sample sintered at 1000 °C, the first infrared peak

moved from 477.95 cm^{-1} to 514.36 cm^{-1}, toward a high wavenumber, resulting in a blue shift. The blue shift of the FT-IR peak was ascribed to the continuous conversion process of monoclinic crystal into tetragonal crystal rendered tetragonal crystal increased in the sintered MgO-PSZ sample. With temperature improving to 1200 °C, the five FT-IR peaks moved to 3447.66 cm^{-1}, 1617.55 cm^{-1}, 1400.37 cm^{-1}, 1066.77 cm^{-1}, and 513.11 cm^{-1}, respectively. Meanwhile, the wavenumbers of the five peaks had not changed much with the comparison to the MgO-PSZ sample sintered at 1100 °C, denoting that the conversion process of m-ZrO_2 into t-ZrO_2 gradually tended to be gentle.

3.3.2 Influence of duration time

Controlling the sintering temperature at 1200 °C and varying holding time among 1 h to 4 h, effects of duration time on the microscopic surface functional groups of the MgO-PSZ samples were presented in Fig. 7. As displayed in Fig. 7, in the magnesia-doped PSZ sample synthesised at 1200 °C, five FT-IR peaks were detected at 3447.66 cm^{-1}, 1617.55 cm^{-1}, 1400.37 cm^{-1}, 1066.77 cm^{-1}, and 513.11 cm^{-1}, respectively. As duration time prolonged to 2 h, the five FT-IR peaks moved to 3447.05 cm^{-1}, 1617.26 cm^{-1}, 1400.37 cm^{-1}, 1066.08 cm^{-1}, and 513.43 cm^{-1}, respectively, with little change; in addition, under the duration time of 3 h, the five peaks correspondingly changed to 3447.28 cm^{-1}, 1617.07 cm^{-1}, 1400.06 cm^{-1}, 1067.88 cm^{-1}, and 513.16 cm^{-1}, without significant change. Similarly, with the duration time prolonging to 4 h, the characteristic peak caused by the Zr-O bonds' stretching vibration moved from 513.16 cm^{-1} to 516.08 cm^{-1}, towards a high wavenumber, resulting in a blue shift. The blue shift indicated that the continuous process of the phase conversion of monoclinic

crystal into tetragonal crystal rendered the increase of the content of tetragonal crystal in the sintered magnesia-doped PSZ sample.

3.4 SEM characterisation

3.4.1 Influence of sintering temperature

SEM images of the synthesised magnesia-doped PSZ samples under various sintering temperatures for 1 h were displayed in Fig. 8, determined using the same magnification of 5000 x. As illustrated in Figs. 8(a) and (b), the surface of the raw fused ZrO_2 sample was smooth, and the particle shape was irregular. After microwave sintering at 900 °C, the sample size became larger and a small number of grains accumulated on the surface (Fig. 8(c)); meanwhile, the particle clumping phenomenon appeared with a temperature rising to 1000 °C, a large number of grains accumulated and the sample began to crystallise (Fig. 8(d)), denoting the phase transition of monoclinic crystal into tetragonal crystal accompanied with the increase of sintering temperature. Additionally, as sintering temperature continually improved to 1100 °C, the edges of the particles began to become smooth, the particles aggregated with each other, and some particles grew abnormally (Fig. 8(e)); furthermore, with temperature reached 1200 °C, the sample surface became smoother, fine grains and no pores arose, and the grain size became more uniform (Fig. 8(f)). The uniform structure of the synthesised magnesia-doped PSZ sample by microwave sintering indicated that the added MgO stabiliser promoted the fusion of crystal grains in ZrO_2 ceramics material, further highlighting that microwave sintering is an effective approach to prepare PSZ ceramics material.

3.4.2 Influence of duration time

SEM images of the synthesised magnesia-doped PSZ samples under microwave radiation at 1200 °C with different durations were presented in Fig. 9, characterised using the same magnification of 5000 x. Under microwave sintering with the duration time of 1 h, a large number of grains were accumulated in the sample, and no pores were generated, as illustrated in Fig. 9(a). Under the duration time of 2 h, there was a partial agglomeration between the grains, and the grain surface became smooth, as illustrated in Fig. 9(b). Besides, as displayed in Fig. 9(c), individual grains in the sample presented prominent growth phenomena with duration time increasing to 3 h. The prominent growth phenomena promoted the grain size to become non-uniform. With duration time continually increasing to 4 h, the grain surface of the synthesised magnesia-doped PSZ sample became smoother, the densification was better, and no pores were generated, as presented in Fig. 9(d). The sintered MgO-PSZ ceramic material with the smoother and denser microstructure indicated microwave sintering approach presented the prominent sintering effect on the fused ZrO_2 material. The approach can be extended to the sintering preparation of other ceramic materials.

4 Conclusions

In the present work, the change in phase, surface morphology, and microstructure of magnesia-doped PSZ ceramics during the microwave sintering process were systematically explored. XRD analysis results denoted that the c-ZrO_2 phase enhanced and the m-ZrO_2 phase gradually weakened until disappeared with the increase of sintering temperature from 900 °C to 1200 °C; however, the m-ZrO_2 phase reappeared with duration time extending, which was

caused by ZrO_2 materials' unique martensitic transformation. Moreover, the conclusions concluded from Raman analysis corresponded to XRD analysis results. Additionally, the reversible martensitic transformation induced a red shift at 1000 ℃ and a blue shift at 1100 ℃ about the FT-IR characteristic peak caused by the Zr-O bonds' contraction vibration. Furthermore, after the raw fused ZrO_2 sample through microwave sintering, the sample surface became smoother surface and the microstructure was more uniformly distributed. This study highlights that microwave sintering means is remarkably effective on the transformation toughening of fused ZrO_2 and the controllable production of high-performance PSZ ceramics.

Acknowledgements

Financial support from National Natural Science Foundation of China (Grant No. 51764052), and Innovative Research Team (in Science and Technology) in the University of Yunnan province.

References

1. C. Patapy, F. Gouraud, M. Huger, R. Guinebretière, B. Ouladiaff, D. Chateigner, T. Chotard, Investigation by neutron diffraction of texture induced by the cooling process of zirconia refractories, J. Eur. Ceram. Soc. 34(15) (2014) 4043-4052. https://doi.org/10.1016/j.jeurceramsoc.2014.05.027.
2. K.Q. Li, Q. Jiang, J. Chen, J.H. Peng, X.P. Li, S. Koppala, M. Omran, G. Chen, The controlled preparation and stability mechanism of partially stabilised zirconia by microwave intensification, Ceram. Int. 46(6) (2020) 7523-7530. https://doi.org/10.1016/j.ceramint.2019.11.251.

3. F. A. Kroger, Electronic conductivity of calcia-stabilised zirconia, J. Am. Ceram. Soc. 49(4) (2010) 215-218. https://doi.org/10.1111/j.1151-2916.1966.tb13237.x.

4. G. Chen, Y.Q. Ling, Q.N. Li, H.W. Zheng, K.Q. Li, Q. Jiang, J. Chen, M. Orman, L. Gao, Crystal structure and thermomechanical properties of CaO-PSZ ceramics synthesised from fused ZrO_2, Ceram. Int. 46(10) (2020) 15357-15363. https://doi.org/10.1016/j.ceramint.2020.03.079.

5. M. Mamivand, M.A. Zaeem, H.E. Kadiri, Effect of variant strain accommodation on the three-dimensional microstructure formation during martensitic transformation: Application to zirconia, Acta. Mater. 87 (2015) 45-55. https://doi.org/10.1016/j.actamat.2014.12.036.

6. X.M. Zeng, A. Lai, C.L. Gan, C.A. Schuh, Crystal orientation dependence of the stress-induced martensitic transformation in zirconia-based shape memory ceramics, Acta. Mater. 116 (2016) 124-135. https://doi.org/10.1016/j.actamat.2016.06.030.

7. Y. Q. Ling, Q. N. Li, H. W. Zheng, M. Omran, L. Gao, J. Chen, G. Chen, Optimisation on the stability of CaO-doped partially stabilised zirconia by microwave heating, Ceram. Int. (2020). https://doi.org/10.1016/ j.ceramint.2020.11.161.

8. K. Q. Li, Q. Jiang, G. Chen, L. Gao, J. H. Peng, Q. Chen, S. Koppala, M. Omran, J. Chen, Kinetics characteristics and microwave reduction behaviour of walnut shell-pyrolusite blends, Bioresour. Technol. 319 (2021) 124172. https://doi.org/10.1016/j.biortech.2020.124172.

9. P.E. Reyes-Morel, I.W. Chen, Transformation plasticity of CeO_2-stabilised tetragonal zirconia polycrystals: I, stress assistance and autocatalysis, J. Am. Ceram. Soc. 71(5) (2010) 343-353. https://doi.org/10.1111/j.1151-2916.1988.tb05052.x.

10. R. Mahendran, S. P. Kumaresh Babu, S. Natarajan, S. Manivannan, A. Vallimanalan, Phase transformation and crystal growth behaviour of 8mol% ($SmO_{1.5}$, $GdO_{1.5}$, and

$YO_{1.5}$) stabilised ZrO_2 powders, Int. J. Miner. Metall. Mater. 24(7) (2017) 842-849. https://doi.org/10.1007/s12613-017-1468-4.

11. G. Chen, Q. N. Li, Y. Q. Ling, H. W. Zheng, J. Chen, Q. Jiang, K. Q. Li, J. H. Peng, M. Omran, L. Gao, Phase stability and microstructure morphology of microwave-sintered magnesia-partially stabilised zirconia, Ceram. Int. (2020). https://doi.org/10.1016/j.ceramint.2020.09.281.
12. G. Chen, Y.Q. Ling, Q.N. Li, H.W. Zheng, K.Q. Li, Q. Jiang, L. Gao, M. Orman, J.H. Peng, J. Chen, Stability properties and structural characteristics of CaO-partially stabilised zirconia ceramics synthesised from fused ZrO_2 by microwave sintering, Ceram. Int. 46(10) (2020) 16842-16848. https://doi.org/10.1016/j.ceramint.2020.03.261.
13. L.L. Fehrenbacher, L.A. Jacobson, Metallographic observation of the monoclinic-tetragonal phase transformation in ZrO_2, J. Am. Ceram. Soc. 48(3) (2010) 157-161. https://doi.org/10.1111/j.1151-2916.1965.tb16054.x.
14. A. Bogicevic, C. Wolverton, G.M. Crosbie, E.B. Stechel, Defect ordering in aliovalently doped cubic zirconia from first principles. Phys. Rev. B. 64(1) (2001) 014106. https://doi.org/10.1103/PhysRevB.64.014106.
15. S. M. Dezfuli, A. Shanaghi, S. Baghshahi, Effect of Al_2O_3 and Y_2O_3 on the corrosion behaviour of ZrO_2-benzotriazole nanostructured coatings applied on AA2024 via a sol-gel method, Int. J. Miner. Metall. Mater. 25(11) (2018) 1344-1353. https://doi.org/10.1007/s12613-018-1688-2.
16. R.C. Garvie, Structure and thermomechanical properties of partially stabilised zirconia in the CaO-ZrO_2 system, J. Am. Ceram. Soc. 55 (2010) 152-157. https://doi.org/10.1007/978-94-009-0741-6_15.

17. R.H.J. Hannink, P.M. Kelly, B.C. Muddle, Transformation toughening in zirconia-containing ceramics, J. Am. Ceram. Soc. 83(3) (2002) 461-487. https://doi.org/10.1111/j.1151-2916.2000.tb01221.x.

18. S. Fabris, A.T. Paxton, M.W. Finnis, A stabilisation mechanism of zirconia based on oxygen vacancies only. Acta. Mater. 50(20) (2002) 5171-5178. https://doi.org/10.1016/S1359-6454(02)00385-3.

19. M.W. Yan, Y. Li, G.X. Yin, S.H. Tong, J.H. Chen, Synthesis and characterisation of a MgO-$MgAl_2O_4$-ZrO_2, composite with a continuous network microstructure, Ceram. Int. 43(8) (2017) 5914-5919. https://doi.org/10.1016/j.ceramint.2017.01.082.

20. K.Q. Li, J. Chen, J.H. Peng, S. Koppala, M. Omran, G. Chen, One-step preparation of CaO-doped partially stabilised zirconia from fused Zirconia, Ceram. Int. 46(5) (2020) 6484-6490. https://doi.org/10.1016/j.ceramint.2019.11.129.

21. K. Chihwei, Y. Shen, F. Yen, H. Cheng, I. Hung, S. Wen, M. Wang, M. Stack, Phase transformation behaviour of 3mol% yttria partially-stabilised ZrO_2 (3Y-PSZ) precursor powder by an isothermal method, Ceram. Int. 40 (2014) 3243-3251 https://doi.org/10.1016/j.ceramint.2013.09.112.

22. E. Tani, M. Yoshimura, S. Somiya, Revised phase diagram of the system ZrO_2-CeO_2 below 1400 °C, J. Am. Ceram. Soc. 66(7) (2010) 506-510. https://doi.org/10.1111/j.1151-2916.1983.tb10591.x.

23. H. Wang, M.H. Wang, W.Y. Zhang, N. Zhao, W. Wei, Y.H. Sun, Synthesis of dimethyl carbonate from propylene carbonate and methanol using CaO-ZrO_2 solid solutions as highly stable catalysts, Catal. Today. 115(1) (2006) 107-110. https://doi.org/10.1016/j.cattod.2006.02.031.

24. H. Wang. M.H Wang, N. Zhao, W. Wei, Y. Sun, CaO-ZrO_2 solid solution: a highly stable catalyst for the synthesis of dimethyl carbonate from propylene carbonate and

methanol, Catal. Lett. 105(3-4) (2005) 253-257. https://doi.org/10.1007/s10562-005-8699-0.

25. B.T. Lin, M.D. Jean, J.H. Chou, Using response surface methodology for optimizing deposited partially stabilised zirconia in plasma spraying, Appl. Surf. Sci. 253 (2007) 3254-3262. https://doi.org/10.1016/j.apsusc.2006.07.021.
26. M.Y. Zhang, L. Gao, J.X. Kang, J. Pu, J.H. Peng, M. Omran, G. Chen, Stability optimisation of CaO-doped partially stabilised zirconia by microwave sintering, Ceram. Int. 45(17) (2019) 23278-23282. https://doi.org/10.1016/j.ceramint.2019.08.024.
27. K.Q. Li, J. Chen, J.H. Peng, R. Ruan, C. Srinivasakannan, G. Chen, Pilot-scale study on enhanced carbothermal reduction of low-grade pyrolusite using microwave heating, Powder. Technol. 360 (2020) 7523-7530. https://doi.org/10.1016/j.powtec.2019.11.015.
28. G. Chen, K.Q. Li, Q. Jiang, X.P. Li, J.H. Peng, M. Omran, J. Chen, Microstructure and enhanced volume density properties of FeMn78C8.0 alloy prepared via a cleaner microwave sintering approach, J. Clean. Prod. 262 (2020) 121364. https://doi.org/10.1016/j.jclepro.2020.121364.
29. K.Q. Li, G. Chen, J. Chen, J.H. Peng, R. Ruan, C. Srinivasakannan, Microwave pyrolysis of walnut shell for reduction process of low-grade pyrolusite, Bioresource. Technol. 291 (2019) 121838. https://doi.org/10.1016/j.biortech.2019.121838.
30. K. Q. Li, J. Chen, J. H. Peng, R. Ruan, M. Omran, G. Chen, Dielectric properties and thermal behaviour of electrolytic manganese anode mud in microwave field, J. Hazard. Mater. 384 (2019) 121227. https://doi.org/10.1016/j.jhazmat.2019.121227.
31. S.H. Guo, G. Chen, J.H. Peng, J. Chen, J.L. Mao, D.B. Li, L.J. Liu, Preparation of partially stabilised zirconia from fused zirconia using sintering, J. Alloy. Compd. 506(1) (2010) L5-L7. https://doi.org/10.1016/j.jallcom.2010.06.156.

32. S.A. Nightingale, H.K. Worner, D.P. Dunne, Microstructural development during the microwave sintering of yttria-zirconia ceramics, J. Am. Ceram. Soc. 80(2) (1997) 394-400. https://doi.org/10.1111/j.1151-2916.1997.tb02843.x.

33. R. Benavente, M.D. Salvador, F.L. Penaranda-Foix, E. Pallone, A. Borrell, Mechanical properties and microstructural evolution of alumina-zirconia nanocomposites by microwave sintering, Ceram. Int. 40(7) (2014) 11291-11297. https://doi.org/10.1016/j.ceramint.2014.03.153.

34. K.Q. Li, G. Chen, X.T. Li, J.H. Peng, R. Ruan, M. Omran, J. Chen, High-temperature dielectric properties and pyrolysis reduction characteristics of different biomass-pyrolusite mixtures in microwave field, Bioresource. Technol. 294 (2019) 122217. https://doi.org/10.1016/j.biortech.2019.122217.

35. M. Mazaheri, A.M. Zahedi, M.M. Hejazi. Processing of nanocrystalline 8 mol% yttria-stabilised zirconia by conventional, microwave-assisted and two-step sintering, Mat. Sci. Eng. A-struct. 492(1) (2008) 261-267. https://doi.org/10.1016/j.msea.2008.03.023.

36. A. K. Behnami, A. Hoseinpur, M. Sakaki, M. S. Bafghi, K. Yanagisawa, Synthesis of WC powder through microwave heating of WO_3-C mixture, Int. J. Miner. Metall. Mater. 24(2) (2017) 202-207. https://doi.org/10.1007/s12613-017-1396-3.

37. K.Q. Li, J. Chen, J.H. Peng, M. Omran, G. Chen, Efficient improvement for dissociation behaviour and thermal decomposition of manganese ore by microwave calcination, J. Clean. Prod. 260 (2020) 121074. https://doi.org/10.1016/j.jclepro.2020.121074.

38. R.R. Thridandapani, C.E. Folgar, A. Kulp, D.C. Folz, D.E. Clark, Effect of direct microwave sintering on structure and properties of 8 Mol% Y_2O_3-ZrO_2, Int. J. Appl. Ceram. Tec. 8(5) (2011) 1229-1236. https://doi.org/10.1111/j.1744-7402.2010.02570.x.

39. P. Liu, L. B. Zhang, B. G. Liu, G. J. He, J. H. Peng, M. Y. Huang, Determination of dielectric properties of titanium carbide fabricated by microwave synthesis with Ti-

bearing blast furnace slag, Int. J. Miner. Metall. Mater. 28(1) (2021) 88-97. https://doi.org/10.1007/s12613-020-1985-4.

40. Y. Murase, E. Kato, K. Daimon, Stability of ZrO_2 phases in ultrafine ZrO_2-Al_2O_3 mixtures, J. Am. Ceram. Soc. 69(2) (1986) 83-87. https://doi.org/10.1111/j.1151-2916.1986.tb04706.x.

Figure captions

Fig. 1 XRD pattern (a) and Raman spectra (b) of the fused ZrO_2 sample.

Fig. 2 XRD patterns of the MgO-PSZ samples sintered at various temperatures for 1 h.

Fig. 3 XRD patterns of the MgO-PSZ samples sintered at 1200 °C under various durations.

Fig. 4 Raman spectra of the MgO-PSZ samples sintered at various temperatures for 1 h, (a) 900 °C; (b) 1000 °C; (c) 1100 °C; (d) 1200 °C.

Fig. 5 Raman spectra of the MgO-PSZ samples sintered at 1200 °C under various durations, (a) 1 h; (b) 2 h; (c) 3 h; (d) 4 h.

Fig. 6 FT-IR spectra of the MgO-PSZ samples sintered at various temperatures for 1 h, (a) 900 °C; (b) 1000 °C; (c) 1100 °C; (d) 1200 °C.

Fig. 7 FT-IR spectra of the MgO-PSZ samples sintered at 1200 °C under various durations, (a) 1 h; (b) 2 h; (c) 3 h; (d) 4 h.

Fig. 8 SEM images of the MgO-PSZ samples sintered at various temperatures for 1 h, (a)-(b) raw material; (c) 900 °C; (d) 1000 °C; (e) 1100 °C; (f) 1200 °C.

Fig. 9 SEM images of the MgO-PSZ samples sintered at 1200 °C under various durations, (a) 1 h; (b) 2 h; (c) 3 h; (d) 4 h.

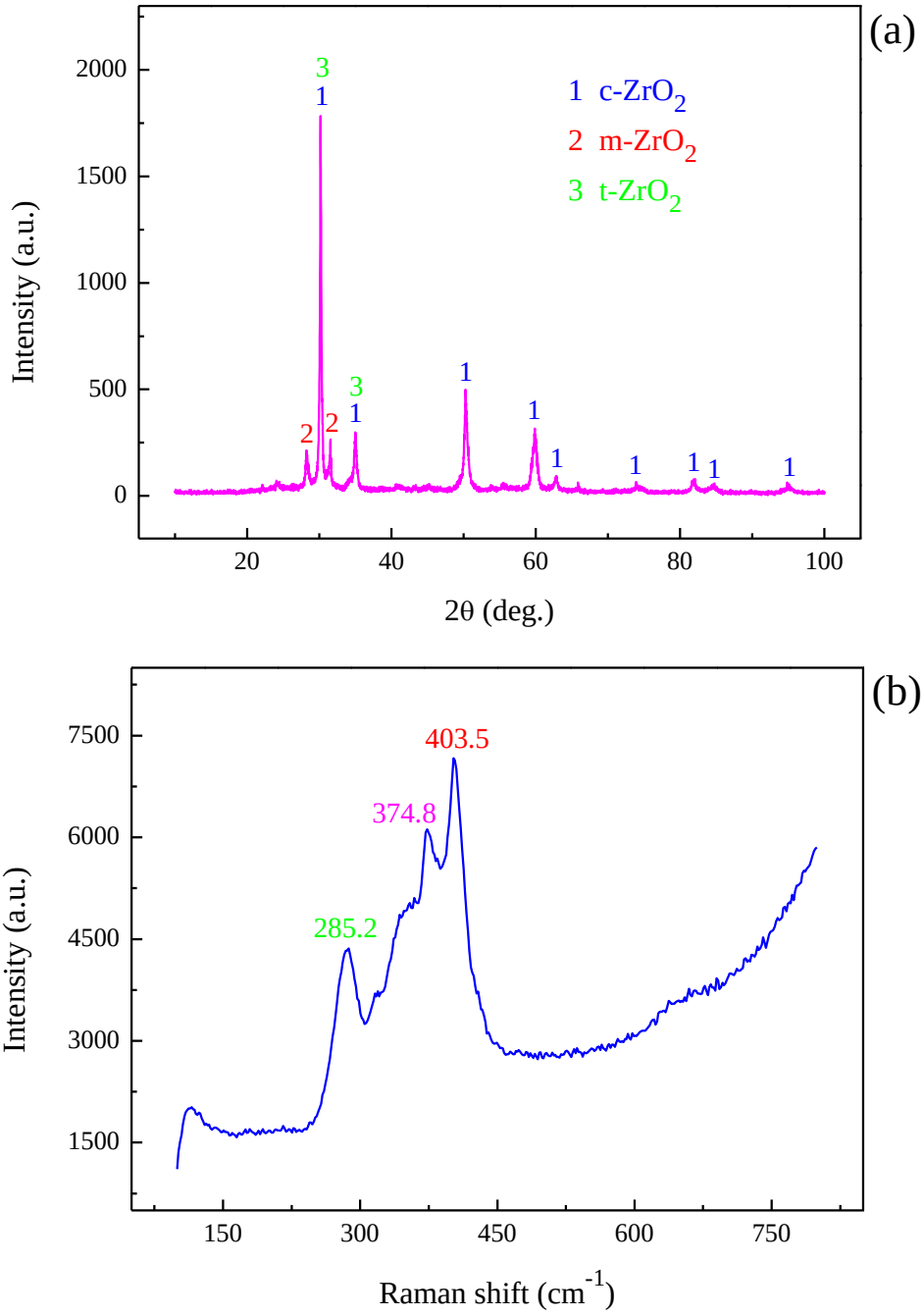

Fig. 1 XRD pattern (a) and Raman spectra (b) of the fused ZrO_2 sample.

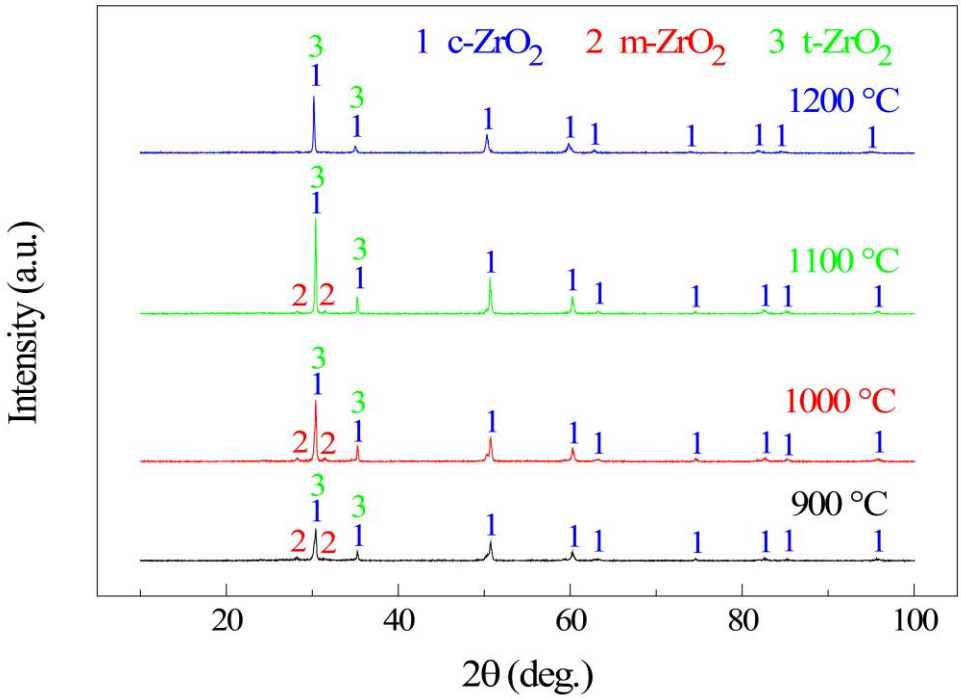

Fig. 2 XRD patterns of the microwave sintered MgO-PSZ samples at various sintering temperatures for 1 h.

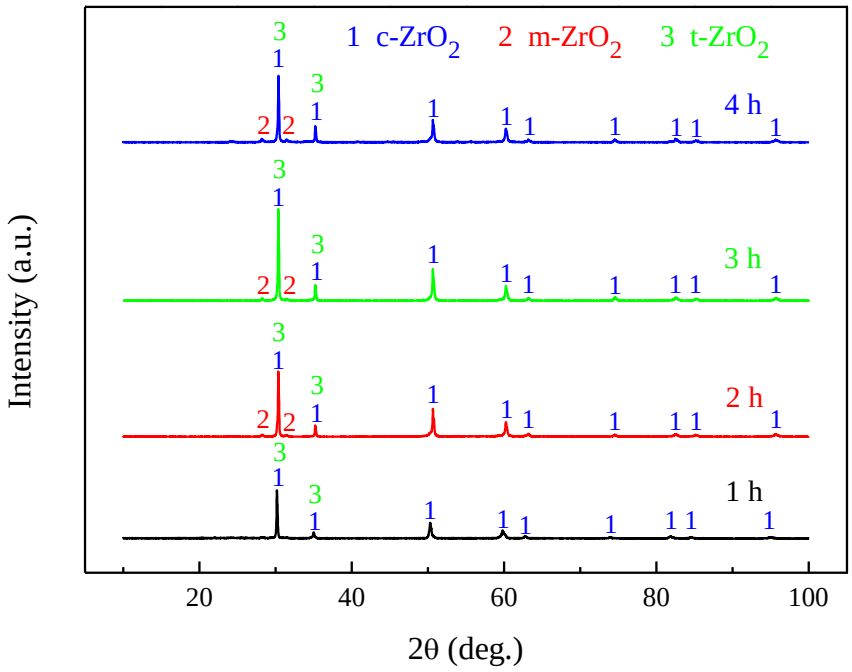

Fig. 3 XRD patterns of the microwave sintered MgO-PSZ samples at 1200 °C under various durations.

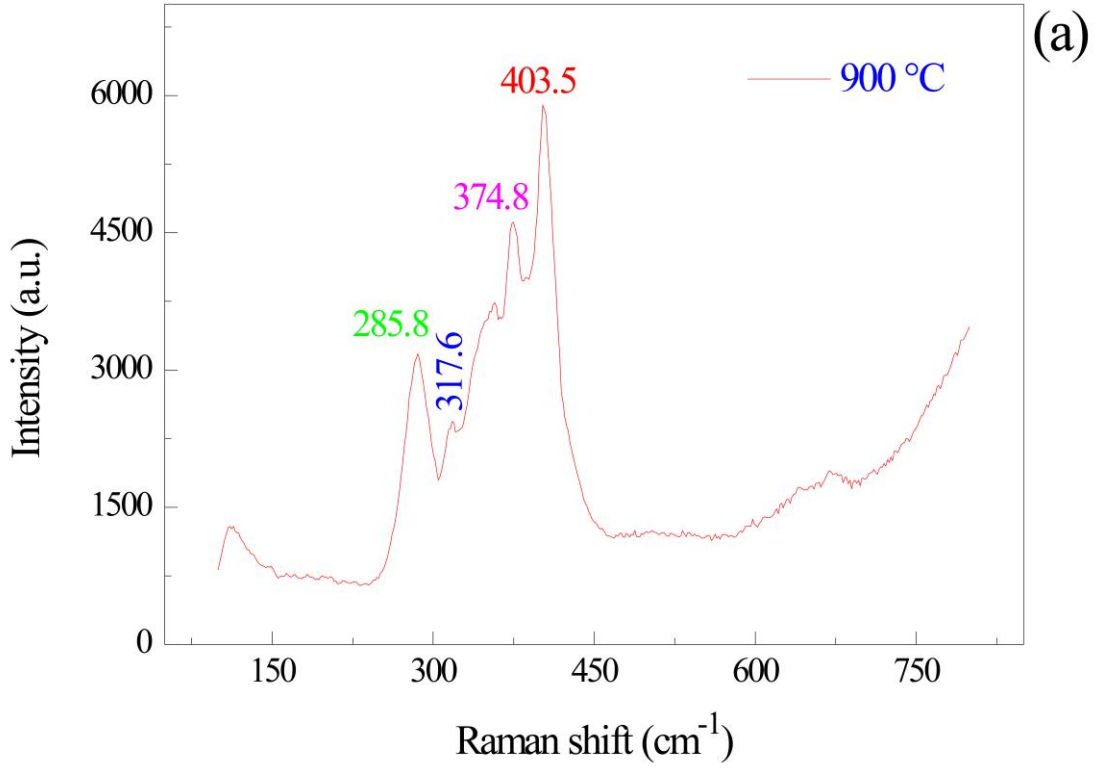
(a)
900 °C
403.5
374.8
285.8
317.6
Intensity (a.u.)
Raman shift (cm-1)
0
1500
3000
4500
6000
150
300
450
600
750

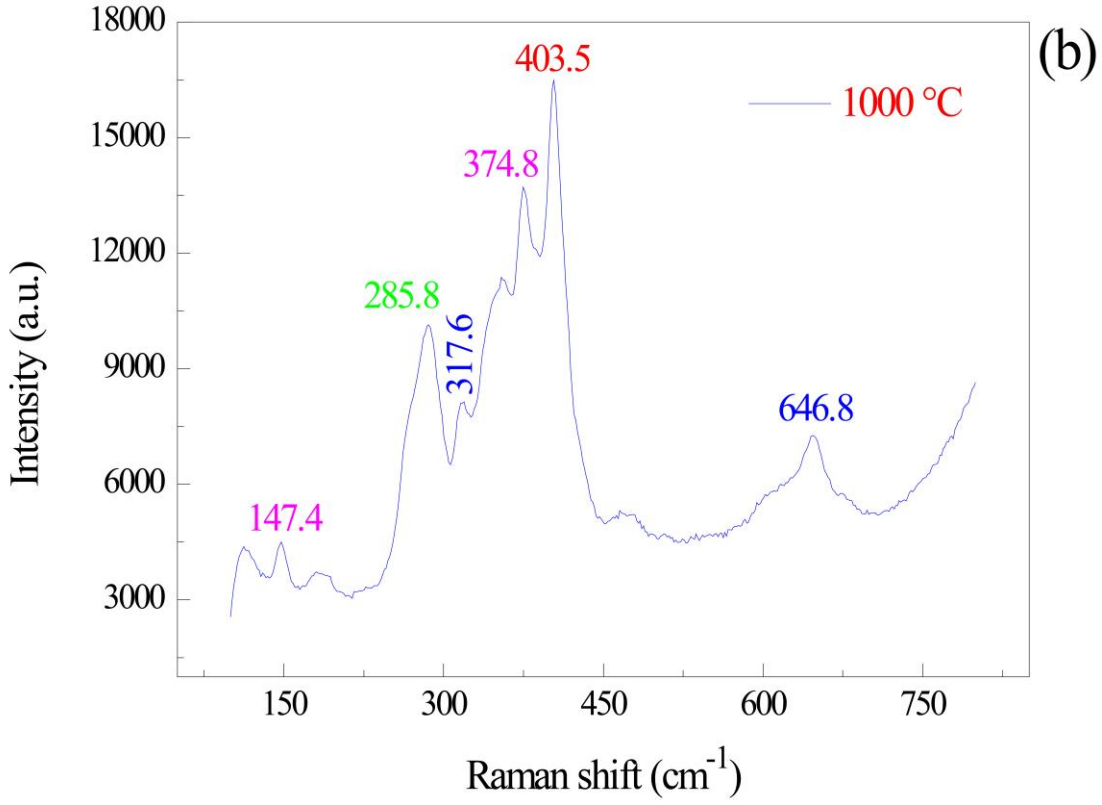
(b)
1000 °C
403.5
374.8
285.8
317.6
646.8
147.4
Intensity (a.u.)
Raman shift (cm-1)
3000
6000
9000
12000
15000
18000
150
300
450
600
750

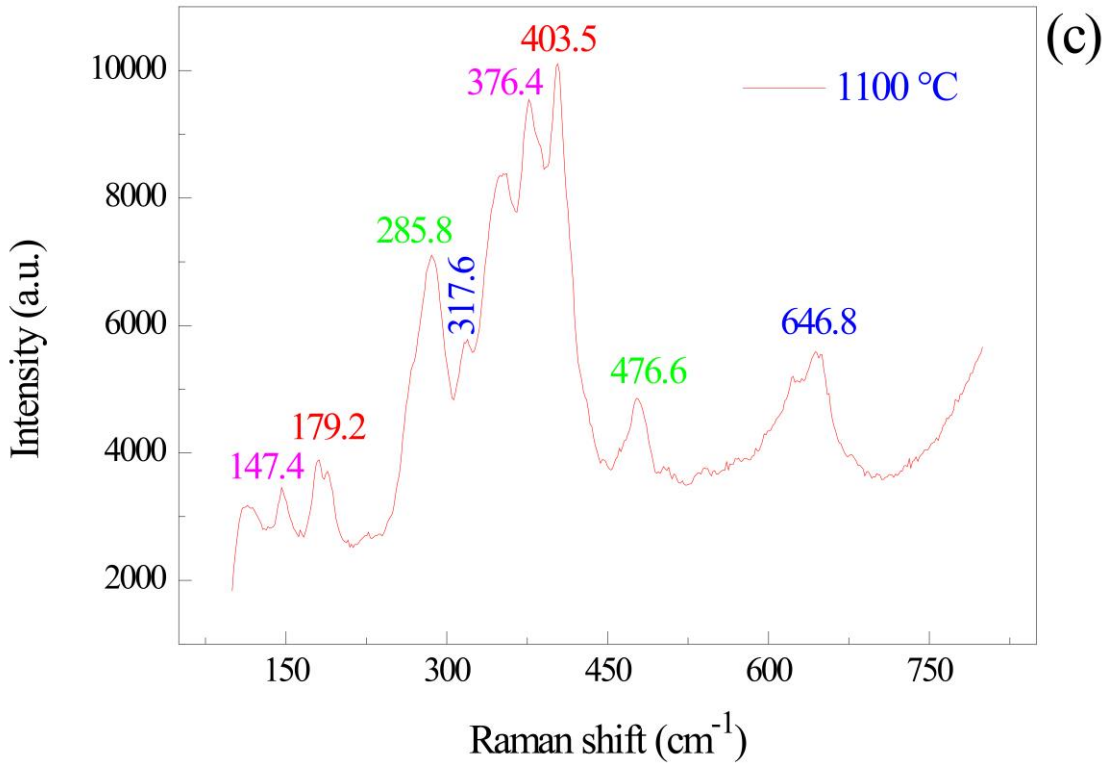

Fig. 4 Raman spectra of the microwave sintered MgO-PSZ samples at various sintering temperatures for 1 h, (a) 900 °C; (b) 1000 °C; (c) 1100 °C; (d) 1200 °C.

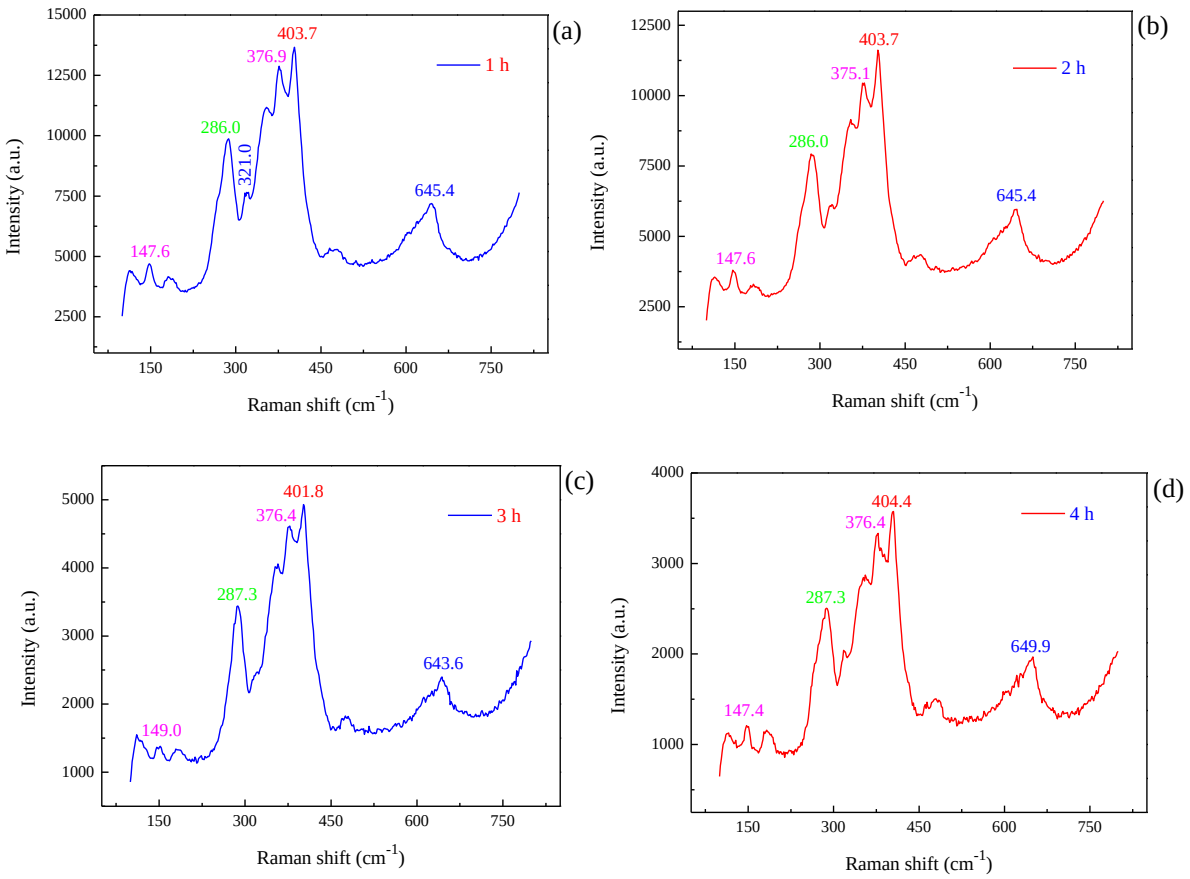

Fig. 5 Raman spectra of the microwave sintered MgO-PSZ samples at 1200 °C under various durations, (a) 1 h; (b) 2 h; (c) 3 h; (d) 4 h.

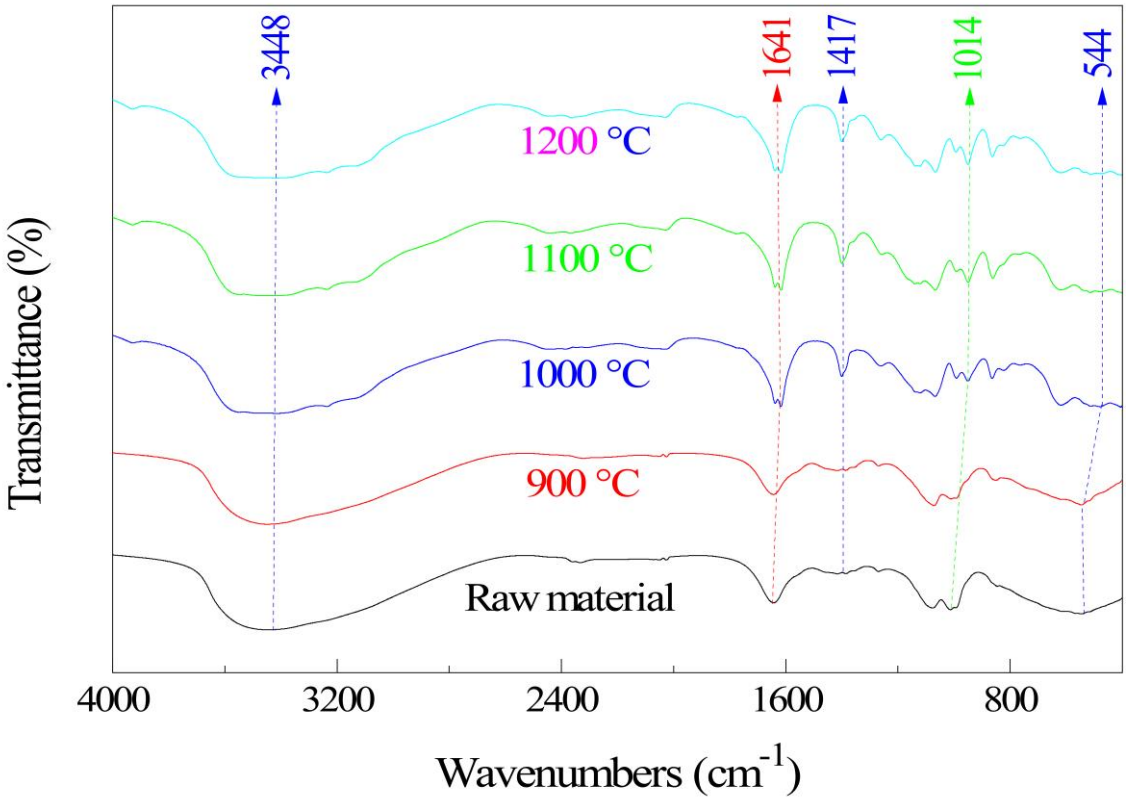

Fig. 6 FT-IR spectra of the microwave sintered MgO-PSZ samples at under various sintering temperatures for 1 h.

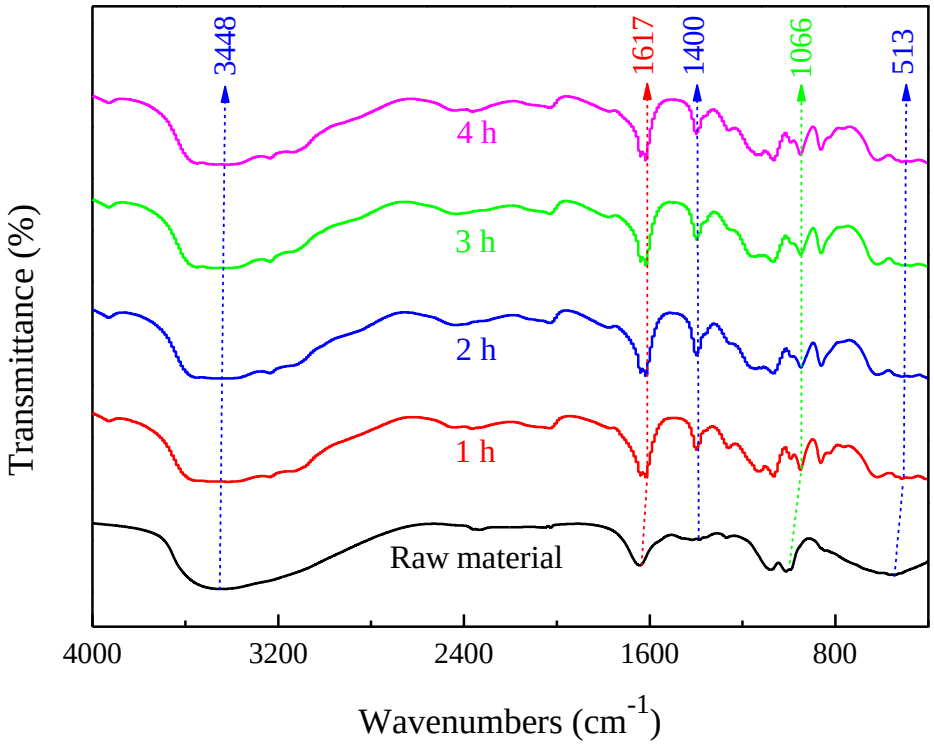

Fig. 7 FT-IR spectra of the microwave sintered MgO-PSZ samples at 1200 °C under various durations.

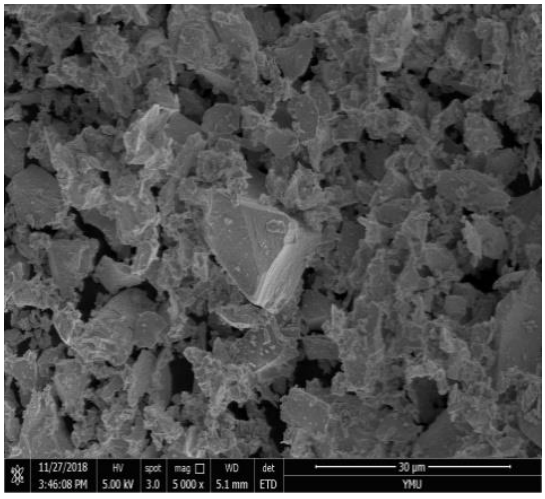
11/27/2018
3:46:08 PM
HV
5.00 kV
spot
3.0
mag
5 000 x
WD
5.1 mm
det
ETD
30 µm
YMU

(a)

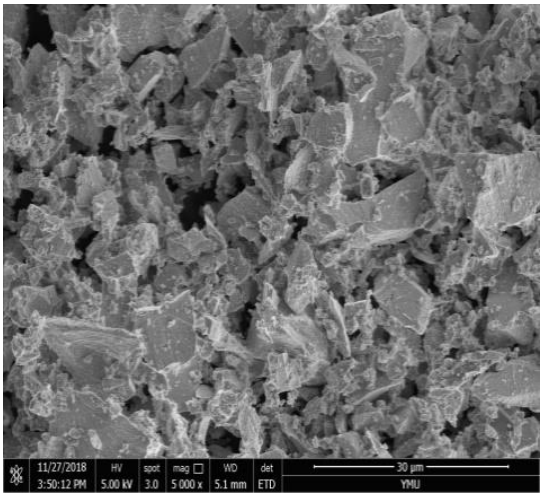
11/27/2018
3:50:12 PM
HV
5.00 kV
spot
3.0
mag
5 000 x
WD
5.1 mm
det
ETD
30 µm
YMU

(b)

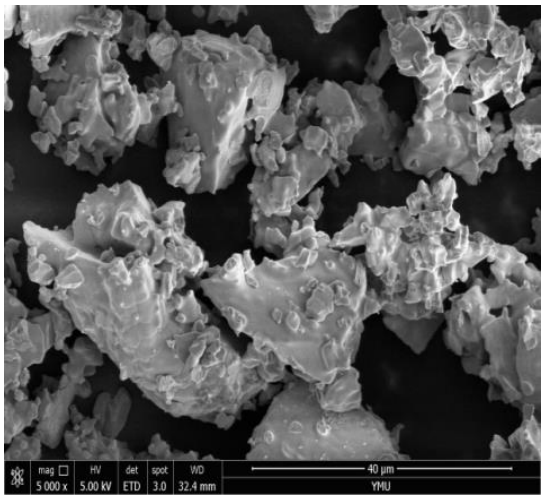
mag
5 000 x
HV
5.00 kV
det
ETD
spot
3.0
WD
32.4 mm
40 µm
YMU

(c)

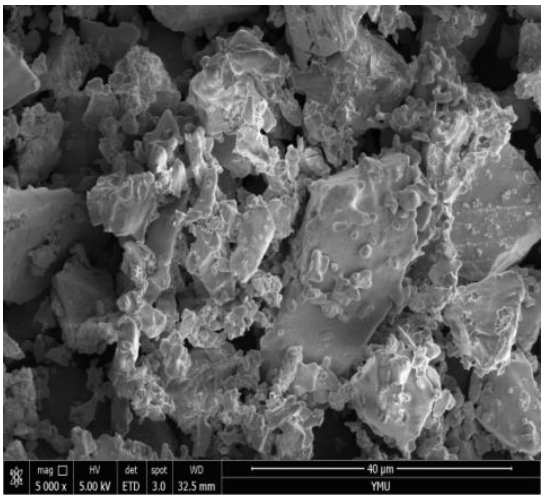
mag
5 000 x
HV
5.00 kV
det
ETD
spot
3.0
WD
32.5 mm
40 µm
YMU

(d)

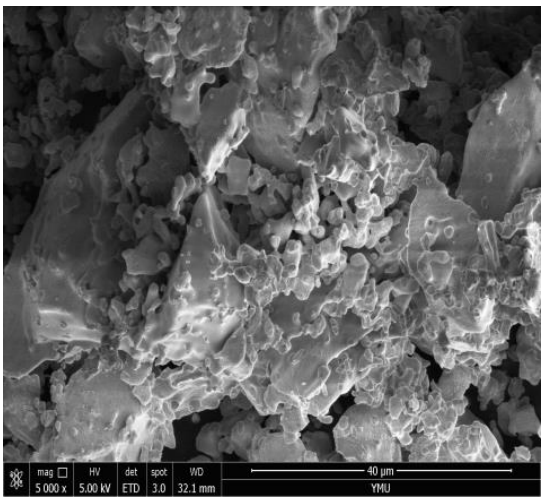
mag
5 000 x
HV
5.00 kV
det
ETD
spot
3.0
WD
32.1 mm
40 µm
YMU

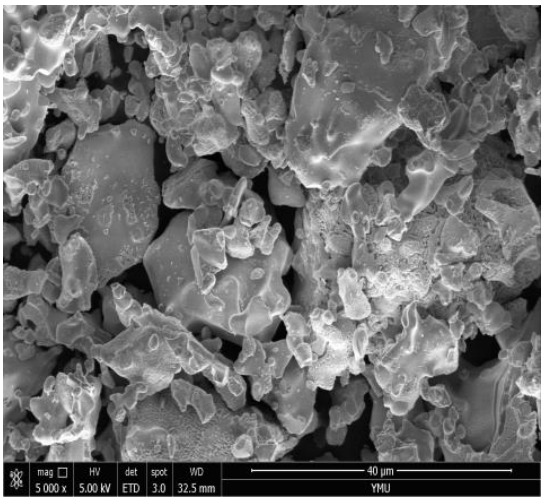
mag
5 000 x
HV
5.00 kV
det
ETD
spot
3.0
WD
32.5 mm
40 µm
YMU

(e) (f)

Fig. 8 SEM images of the microwave sintered MgO-PSZ samples at various sintering temperatures for 1 h, (a)-(b) raw material; (c) 900 °C; (d) 1000 °C; (e) 1100 °C; (f) 1200 °C.

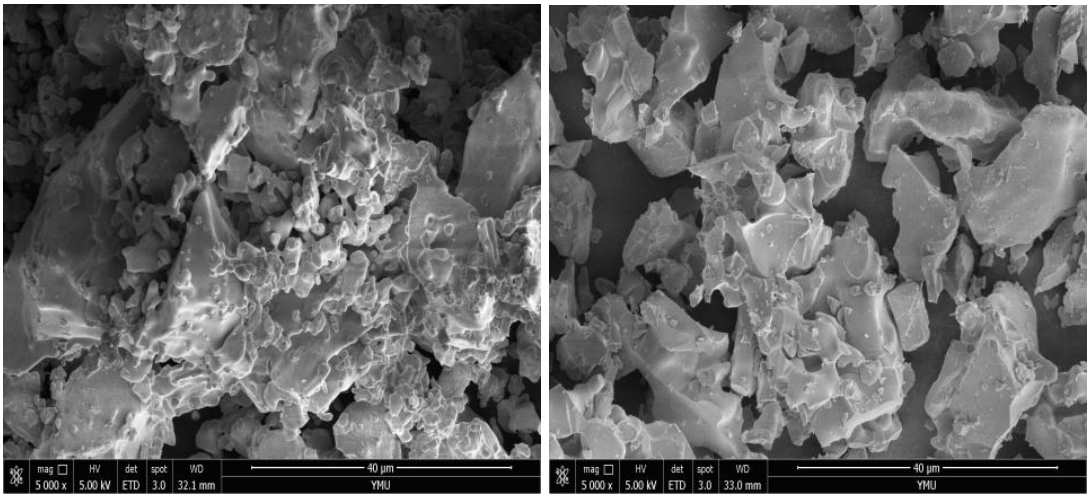

(a) (b)

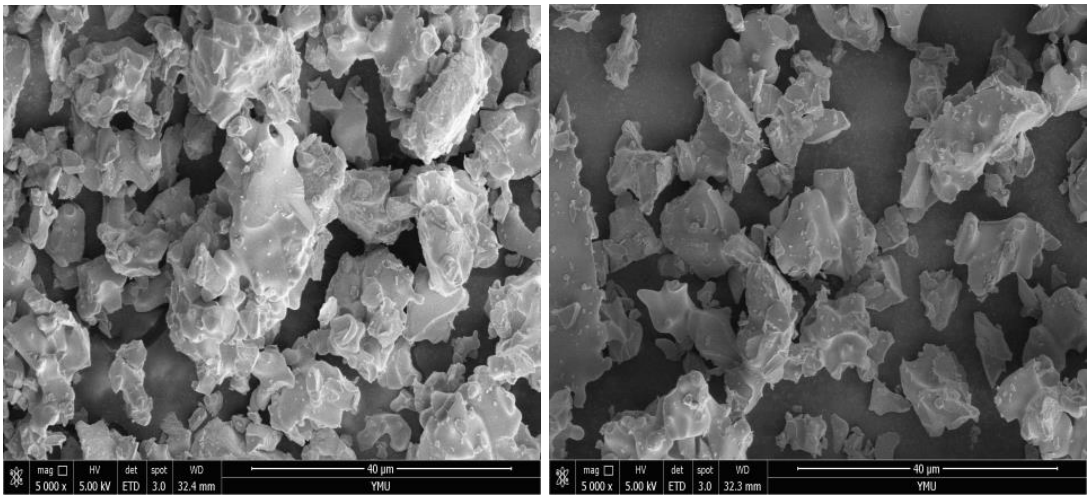

(c) (d)

Fig. 9 SEM images of the microwave sintered MgO-PSZ samples at 1200 °C under various durations, (a) 1 h; (b) 2 h; (c) 3 h; (d) 4 h.